Supplementary Information

# Anisotropic charge trapping in phototransistors unlocks ultrasensitive polarimetry

**Jing Pan[1#], Xiujuan Zhang[1#], Yiming Wu[3], Jinhui Chen[1], Jinwen Wang[1], Shuiling Cheng[1], Xiaofeng Wu[1], Xiaohong Zhang[1], and Jiansheng Jie[1,2]***

[1]Institute of Functional Nano & Soft Materials (FUNSOM), Jiangsu Key Laboratory for Carbon-Based Functional Materials & Devices, Soochow University, Suzhou, Jiangsu 215123, P. R. China

[2]Macao Institute of Materials Science and Engineering, Macau University of Science and Technology, Taipa, Macau SAR 999078, P. R. China

[3]Institute of Materials Research and Engineering, Agency for Science, Technology and Research (A*STAR), Singapore 138634, Singapore

#These authors contributed equally: Jing Pan, Xiujuan Zhang

*E-mail: jsjie@suda.edu.cn

**Table of Contents**

## I. Compact model of organic field-effect transistors

We utilize the compact model of organic field-effect transistors (OFETs) developed by Estrada *et al.*[1,2] to simulate the transfer characteristics of a phototransistor. The model can well explain the drain current ($I_{DS}$) both in the above-threshold regime and the sub-threshold regime. The above-threshold drain current ($I_{above}$) of a p-type OFET can be described as the product of three parts: channel conductance ($g_{ch}$), effective drain voltage ($V_{DSe}$) for a smooth linear-to-saturation transition, and a modified asymptotic expression $[1+\lambda_s(|V_{DS}|-\alpha_s|V_G-V_{th}|)]$ for better describing the output conductance:

$$I_{above} = g_{ch} V_{DSe}[1+\lambda_s(|V_{DS}|-\alpha_s|V_G-V_{th}|)]$$

$$= -\frac{\frac{W}{L}C_i\mu_{FET}(V_G-V_{th})}{1-R_c[\frac{W}{L}C_i\mu_{FET}(V_G-V_{th})]} \cdot \frac{V_{DS}[1+\lambda_s(|V_{DS}|-\alpha_s|V_G-V_{th}|)]}{[1+|\frac{V_{DS}}{\alpha_s(V_G-V_{th})}|^m]^{\frac{1}{m}}} \quad \text{(S1)}$$

where $W$ and $L$ are the channel width and length of the device, respectively, $C_i$ is the unit-area capacitance of the dielectric layer, $\mu_{FET}$ is the field-effect mobility, $V_G$ is the gate voltage, $V_{th}$ is the threshold voltage, $V_{DS}$ is the drain voltage, $R_c$ is the contact resistance, $m$ is the linear-to-saturation transition parameter, $\lambda_s$ is the saturation coefficient, and $\alpha_s$ is the saturation modulation parameter. For simplicity, we now consider an ideal case where $R_c = 0$, and a $V_G$-independent intrinsic mobility of the active material ($\mu_{in}$) is used instead of $\mu_{FET}$. $I_{above}$ can thus be written as:

$$I_{above} \approx \frac{-\frac{W}{L}C_i\mu_{in}(V_G-V_{th})V_{DS}[1+\lambda_s(|V_{DS}|-\alpha_s|V_G-V_{th}|)]}{[1+|\frac{V_{DS}}{\alpha_s(V_G-V_{th})}|^m]^{\frac{1}{m}}} \quad \text{(S2)}$$

The sub-threshold drain current ($I_{sub}$) can be expressed as:

$$I_{sub} = I_0 \exp[-\frac{\ln 10}{SS}(V_G-V_{on})] \quad \text{(S3)}$$

where $I_0$ is the off-state current, $SS$ is the subthreshold swing, and $V_{on}$ is the onset voltage. A hyperbolic tangent transition function is used to combine the two regimes together. The total $I_{DS}$ is:

$$I_{\text{total}} = I_{\text{above}} \cdot \frac{1}{2}[1-\tanh[B(V_{\text{G}}-V_{\text{B}})]] + I_{\text{sub}} \cdot \frac{1}{2}[1+\tanh[B(V_{\text{G}}-V_{\text{B}})]] + I_0 \qquad \text{(S4)}$$

Note that here two additional parameters, namely transition voltage ($V_{\text{B}}$) and transition parameter ($B$) are used for smooth transition between $I_{\text{above}}$ and $I_{\text{sub}}$. Because $I_{\text{above}}$ exhibits a steep drop when approaching $V_{\text{th}}$, $V_{\text{B}}$ is normally chosen to be a few volts away from $V_{\text{th}}$ toward the above-threshold direction for a better transition. Supplementary Table 1 lists the values of the parameters used for describing an ideal OFET, note that the values of $W$, $L$, $C_{\text{i}}$ are based on the device structure of our organic phototransistor (OPT), and other values were set carefully to ensure a smooth and ideal transfer curve[1] (Supplementary Fig. 1).

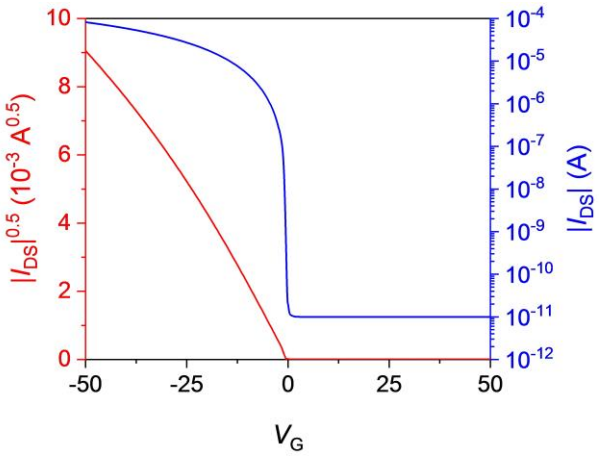


**Supplementary Figure 1 |** Transfer characteristics of an ideal OFET described by the compact model.

**Supplementary Table 1** | Parameters used for describing an ideal OFET.

| Parameter | Value | Note |
|---|---|---|
| $W$ | 75 μm | Channel width |
| $L$ | 25 μm | Channel length |
| $C_i$ | $1.8\times10^{-8}$ F cm$^{-2}$ | Capacitance of a 200 nm-thick $SiO_2$ layer |
| $\mu_{in}$ | 1 cm$^2$ V$^{-1}$ s$^{-1}$ | Intrinsic mobility |
| $V_{th}$ | 0 V | Threshold voltage |
| $V_{on}$ | 0 V | Onset voltage |
| $\lambda_s$ | $-1\times10^{-3}$ V$^{-1}$ | Saturation coefficient |
| $\alpha_s$ | 1 | Saturation modulation parameter |
| $m$ | 1.8 | Linear-to-saturation transition parameter |
| $SS$ | 1 V dec$^{-1}$ | Subthreshold swing |
| $I_0$ | $-1\times10^{-11}$ A | Off-state current |
| $B$ | 3 V$^{-1}$ | Below-to-above-threshold transition parameter |
| $V_B$ | -1 V | Transition voltage |

## II. Working modes of phototransistors

Generally, there are two working modes in a phototransistor, namely the photoconductive (PC) mode and the photovoltaic (PV) mode[3]. The PC mode is related to the change of the channel conductance due to the difference in charge carrier concentration upon light illumination. Therefore, in an ideal PC mode where photogenerated electrons and holes are effectively separated under the electric field, and are totally collected by the electrodes before recombination, the photocurrent ($I_{ph}$) is linearly proportional to the incident light power ($P$) (Supplementary Fig. 2), and can be described as:

$$I_{ph,PC} = (q\mu nE)WD = \beta P \tag{S5}$$

where $q$ is the elementary charge, $\mu$ is the mobility of majority charge carriers, $n$ is the charge concentration, $E$ is the electric field along the channel, $D$ is the depth of the absorption region, and $\beta$ is a proportionality parameter.

The PV mode of a phototransistor is related to the change of $V_{th}$, which is also described as the photogating effect[4]. Practically, the existence of trap sites in the interface or contact regions can lead to trapping and accumulation of minority charge carriers, which lowers the injection barrier of majority charge carriers. With the trapped minority charge carriers functioning as a localized gate, the excess majority charge carriers can drift in the channel several times before recombination, resulting in a high current gain. The threshold voltage shift ($\Delta V_{th}$) in a photogating process can be expressed as:

$$\Delta V_{th} = \frac{NkT}{q}\ln(1+\frac{\eta q\lambda P}{I_d hc}) \tag{S6}$$

where $N$ is an empirical parameter, $k$ is the Boltzmann constant, $T$ is the temperature, $\eta$ is the quantum efficiency of photogeneration, $\lambda$ is the wavelength of the incident light, $I_d$ is the dark current of minority charge carriers, $h$ is the Planck's constant, and $c$ is the speed of light in vacuum. The photocurrent in the PV mode is:

$$I_{ph,PV} = g_m \Delta V_{th} = \frac{AkT}{q}\ln(1+\frac{\eta q\lambda P}{I_d hc}) \tag{S7}$$

where $g_m$ is the transconductance, and $A$ is a proportionality parameter.

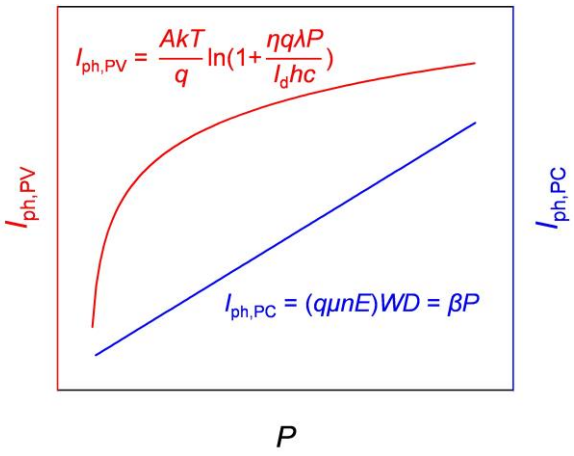


**Supplementary Figure 2 |** Plots of light power-dependent $I_{ph}$ in PC (blue curve) and PV (red curve) modes of a phototransistor.

## III. Theoretical estimation of the polarization-dependent photogating effect

Here we analyze the great difference between PC and PV modes, and give a reasonable prediction of to what extent the polarization-dependent photogating (PDPG) effect can enhance the polarization sensitivity by simulating the drift of transfer curves of a phototransistor under polarized light.

In an ideal PC mode, $I_{ph}$ increases linearly with the amount of light absorbed. Therefore, assuming the device is illuminated by a parallelly ( $\parallel$ ) or perpendicularly ($\perp$) polarized light with the electric field $\boldsymbol{E}_{\parallel}$ or $\boldsymbol{E}_{\perp}$ orienting to the strongest or weakest light absorption direction, respectively, the anisotropic ratio of light absorption should determine the upper limit of the dichroic ratio of the channel current (DR = $I_{\text{light},\parallel}/I_{\text{light},\perp}$).

In terms of the PV mode, the anisotropic light absorption will result in the difference in the number of trapped charge carriers and polarization-dependent shift of $V_{th}$. We utilize the values listed in Supplementary Table 2 to predict $\Delta V_{th}$ under polarized light. The value of the empirical parameter $N$ is selected based on the fitting curve for the experimental data in Supplementary Fig. 16d. For a photoactive crystal with an absorption anisotropic ratio of $a_{in}$ ($a_{in} > 1$), ideally with the quantum efficiency $\eta = 1$, it will lead to varied number of photogenerated charge carriers in different polarization states, which can be analogous to the result of changing $P$ of an unpolarized light (*i.e.*, $P$ and $a_{in}P$). Therefore, the $P$-related expression (Equation S6) is used to describe $\Delta V_{th}$ caused by anisotropic charge trapping. For $\boldsymbol{E}_{\parallel}$ we can write down:

$$\Delta V_{\text{th},\parallel} = \frac{775.6\times(1.38\times10^{-23}\ \text{JK}^{-1})\times(298.15\,\text{K})}{1.6\times10^{-19}\,\text{C}}\ln[1+\frac{(1.6\times10^{-19}\,\text{C})\times(365\times10^{-9}\ \text{m})\times a_{in}P}{(5\times10^{-11}\ \text{A})\times(6.626\times10^{-34}\,\text{Js})\times(3\times10^{8}\ \text{ms}^{-1})}] \quad \text{(S8)}$$

for $\boldsymbol{E}_{\perp}$ we have

$$\Delta V_{\text{th},\perp} = \frac{775.6\times(1.38\times10^{-23}\ \text{JK}^{-1})\times(298.15\,\text{K})}{1.6\times10^{-19}\,\text{C}}\ln[1+\frac{(1.6\times10^{-19}\,\text{C})\times(365\times10^{-9}\ \text{m})\times P}{(5\times10^{-11}\ \text{A})\times(6.626\times10^{-34}\,\text{Js})\times(3\times10^{8}\ \text{ms}^{-1})}] \quad \text{(S9)}$$

The threshold voltage difference between the two polarization states is thus,

$$\Delta V_{\mathrm{th,PDPG}} = \Delta V_{\mathrm{th},\parallel} - \Delta V_{\mathrm{th},\perp} = 19.94 \times \ln\left(\frac{1 + 5.88 \times 10^{9} \times a_{\mathrm{in}} P}{1 + 5.88 \times 10^{9} \times P}\right) \ \mathrm{V} \qquad \text{(S10)}$$

According to the above equation, as $P$ increases, $\Delta V_{\mathrm{th,PDPG}}$ will gradually approach a constant value (Supplementary Fig. 4a). Therefore, for a particular $a_{\mathrm{in}}$, we can predict the upper limit of $\Delta V_{\mathrm{th,PDPG}}$ that can be obtained. *E.g.*, for C8-BTBT crystals we used for fabricating OPTs in following discussions, the maximum $\Delta V_{\mathrm{th,PDPG}}$ is estimated to be ~34.2 V with $a_{\mathrm{in}} = 5.6$ (Supplementary Fig. 4b). Since our estimations are based not on the absolute value of $V_{\mathrm{th}}$ but on the change in $V_{\mathrm{th}}$ under polarized light, the exact position of threshold/onset point in the dark does not impact our conclusions. Therefore, we utilize the compact model in Section I and assign the threshold/onset point of $I_{\mathrm{light},\perp}$ as reference zero. The relative value of $I_{\mathrm{light},\parallel}$ can be attained with $\Delta V_{\mathrm{th,PDPG}} = \Delta V_{\mathrm{on,PDPG}} = \Delta V_{\mathrm{B,PDPG}} = 34.2$ V, and further the $a_{\mathrm{in}}$-related DR can be predicted. Note that the subthreshold current $I_0$ may be higher under light illumination due to the generation of excess charge carriers. Therefore, $I_0$ is set to be $10^{-9}$ A for a more accurate prediction in the practical case. The DR can reach over $10^4$ in PV mode compared to the limited value (DR $\leq$ 5.6) in PC mode (Supplementary Fig. 5a). Further, it is suggested that fabricating high-quality photoactive crystals with a larger $\mu_{\mathrm{in}}$ is favorable for attaining a much higher DR (Supplementary Fig. 5b).

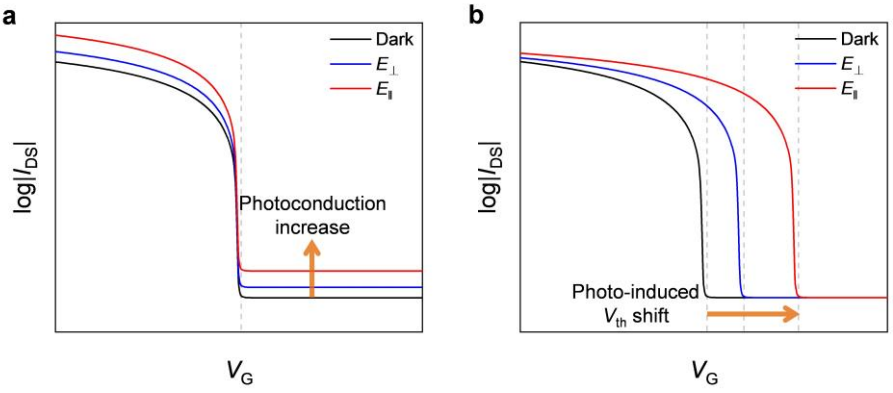


**Supplementary Figure 3 |** Schematics of polarization-dependent transfer curves of a phototransistor ideally working in **a,** PC mode and **b,** PV mode.

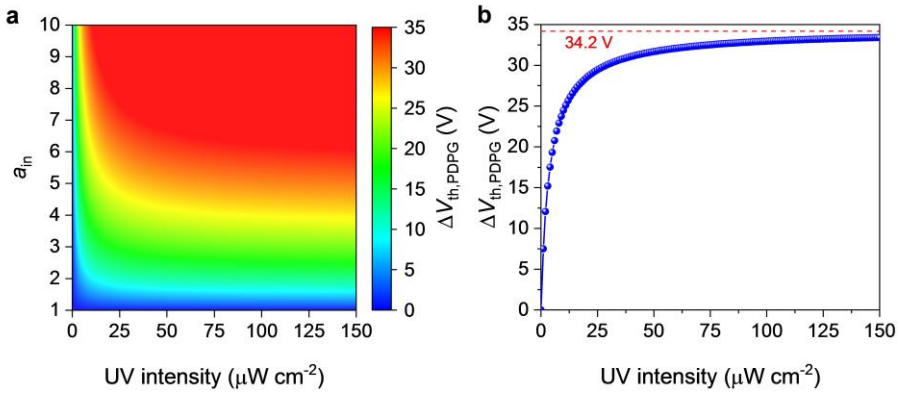


153

154 **Supplementary Figure 4 | a,** Contour plot of predicted $\Delta V_{th,PDPG}$ *versus* $a_{in}$ and UV

155 intensity. **b,** Predicted relationship between $\Delta V_{th,PDPG}$ and UV intensity with $a_{in}$ = 5.6.

156

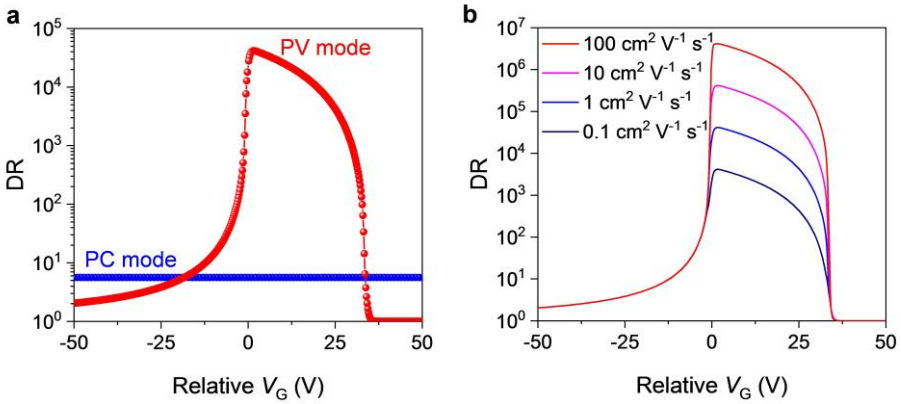


157

158 **Supplementary Figure 5 | a,** Predicted DRs in PC mode (blue curve) and PV mode

159 (red curve) of a phototransistor with $\mu_{in}$ = 1 cm$^2$ V$^{-1}$ s$^{-1}$ and $a_{in}$ = 5.6. **b,** Predicted

160 influence of $\mu_{in}$ on DR ($a_{in}$ = 5.6). The relative $V_G$ represents the applied gate voltage

161 relative to the reference threshold/onset point of $I_{light,\perp}$.

162

**Supplementary Table 2** | Parameters used for describing $\Delta V_{th}$ caused by the photogating effect.

| Parameters | Value | Note |
|---|---|---|
| $W \times L$ | $75 \times 25\ \mu m^2$ | Device area |
| $N$ | 775.6 | Fitted empirical parameter |
| $k$ | $1.38 \times 10^{-23}$ J K$^{-1}$ | Boltzmann constant |
| $T$ | 298.15 K | Room temperature |
| $q$ | $1.6 \times 10^{-19}$ C | Elementary charge |
| $\lambda$ | 365 nm | Incident light wavelength |
| $I_d$ | $5 \times 10^{-11}$ A | Dark current in the off-state |
| $h$ | $6.626 \times 10^{-34}$ J s | Planck's constant |
| $c$ | $3 \times 10^{8}$ m s$^{-1}$ | Speed of light |

**Supplementary Table 3** | Comparison of anisotropic photoactive crystals in previous reports. The intrinsic anisotropic ratio here refers to the anisotropic ratio of light absorption.

| Material | $\lambda$ (nm) | $a_{in}$ | Ref. |
|---|---|---|---|
| **C8-BTBT** | **365** | **5.6** | **This work** |
| GeSe | 808 | 3.02 | [5] |
| Te | 2300-3300 | ~10 | [6] |
| $SbI_3 \cdot 3S_8$ | 430 | 3.9 | [7] |
| $CsPbBr_3$ | ~517 | 2.8 | [8] |
| $(BA)_2(MA)Pb_2Br_7$ | 405 | 1.9 | [9] |
| DPA | 436 | 3.97 | [10] |

## IV. Fabrication and characterizations of C8-BTBT crystal array

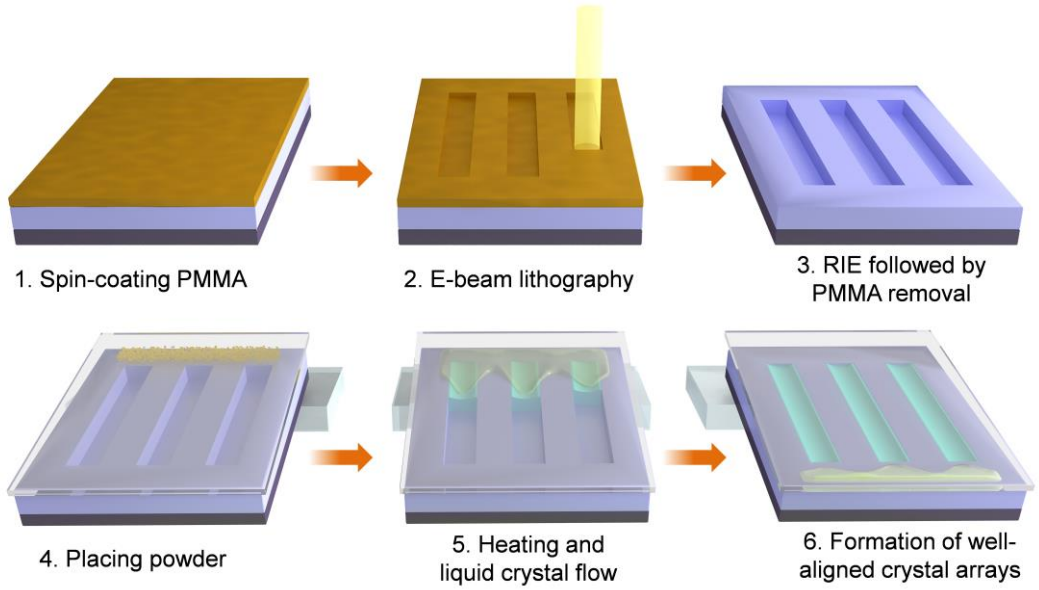


**Supplementary Figure 6 |** Schematics of the fabrication process of C8-BTBT crystal array.

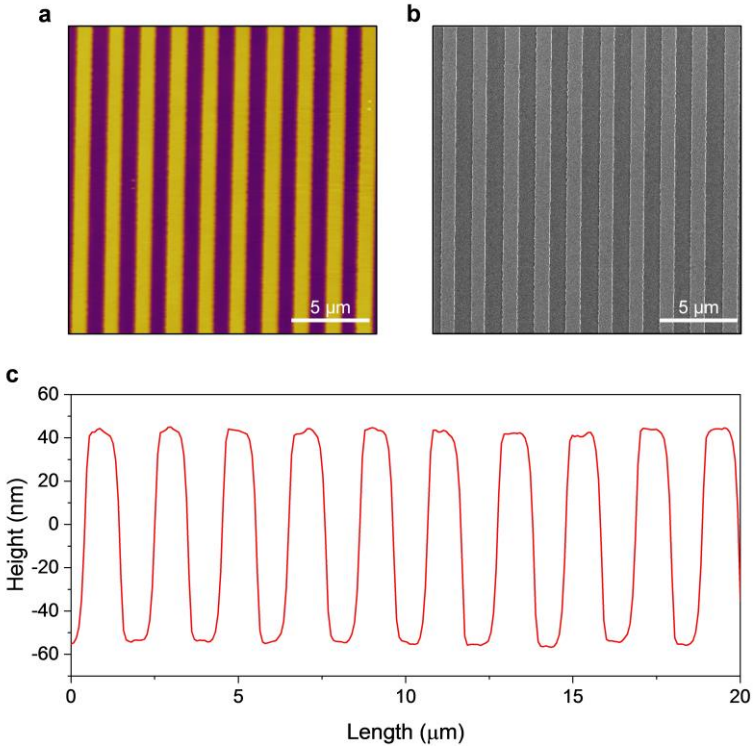


**Supplementary Figure 7 | a,** AFM and **b,** SEM characterizations of the periodic $SiO_2$ micro-channels. **c,** Corresponding height profile of the $SiO_2$ micro-channels. The height and width of the channel are ~100 nm and ~1 μm, respectively.

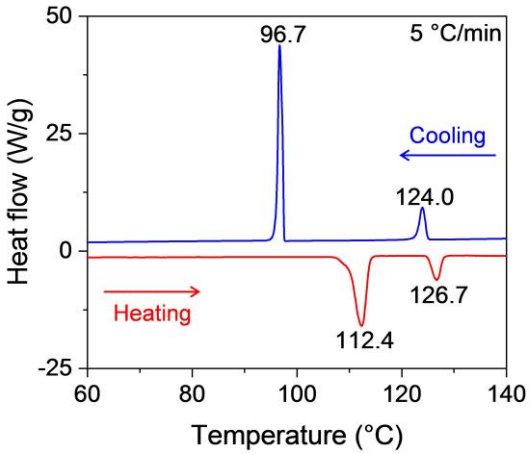


**Supplementary Figure 8 |** Difference scanning calorimeter thermogram of C8-BTBT powder. The heating and cooling speed is set to be 5°C/min. The smectic liquid crystal phase and the isotropic phase of C8-BTBT appears at 112.4°C and 126.7°C upon heating, respectively. Therefore, a heating temperature of 130°C is used to acquire free-flowing C8-BTBT liquid for channel-restricted growth.

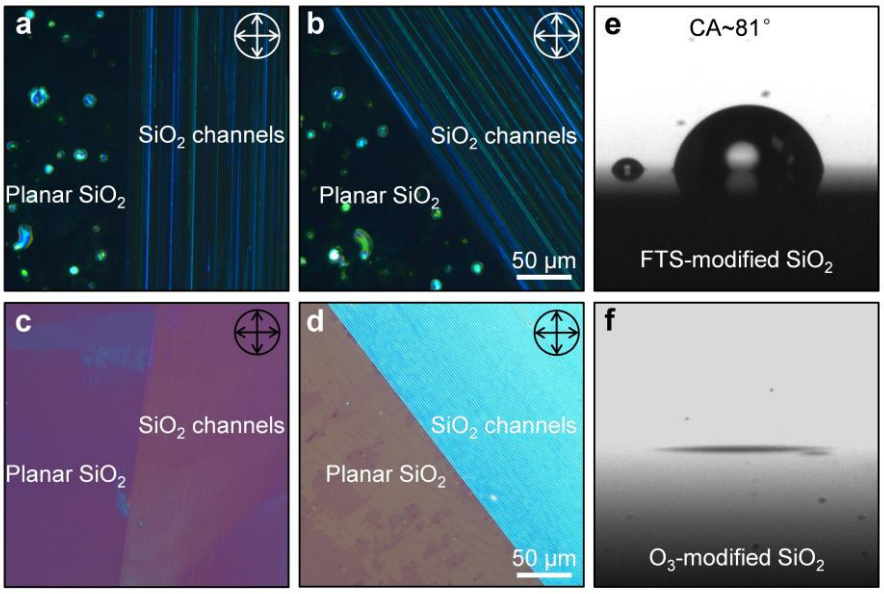


**Supplementary Figure 9 |** Cross-polarized optical microscopy images of C8-BTBT grown on **a-b,** FTS-modified and **c-d,** $O_3$-modified $SiO_2$ templates. Contact angle (CA) measurements of the C8-BTBT liquid droplet on **e,** FTS-modified and **f,** $O_3$-modified $SiO_2$ templates. The surface modification was found to have a large influence on the flow of C8-BTBT liquid. Lyophobic treatment by FTS (CA~81°) results in the pinning of C8-BTBT liquid droplets on $SiO_2$ and differently oriented C8-BTBT polycrystals after cooling, while lyophilic treatment by $O_3$ (negligible CA) can lead to free-flowing C8-BTBT liquid on $SiO_2$ and uniformly oriented C8-BTBT crystals after cooling.

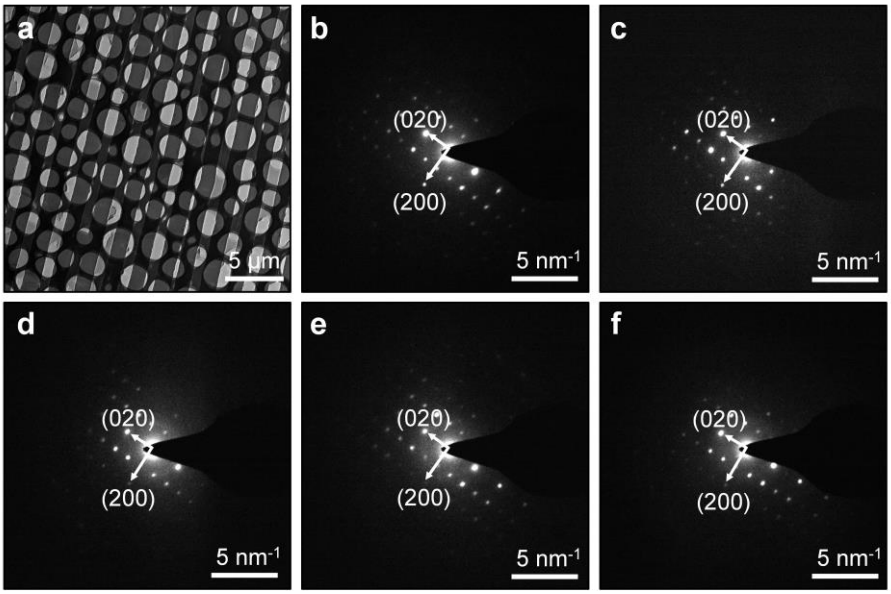


197

198 **Supplementary Figure 10 | a,** TEM image and **b-f,** the corresponding electron

199 diffraction patterns of the C8-BTBT crystal array.

200

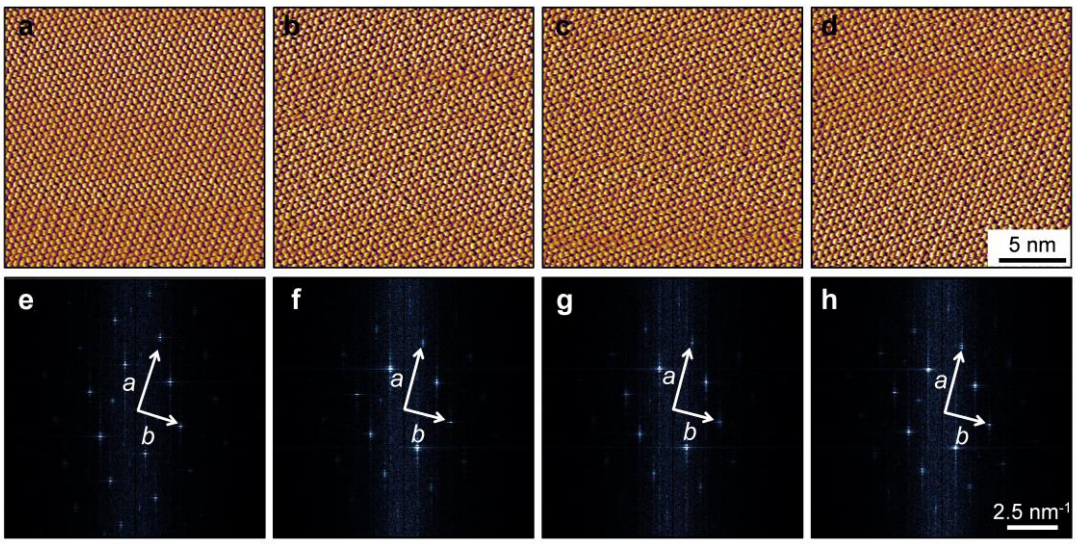


201

202 **Supplementary Figure 11 | a-d,** High-resolution AFM images and **e-h,** the

203 corresponding FFT patterns of the C8-BTBT crystal array.

204

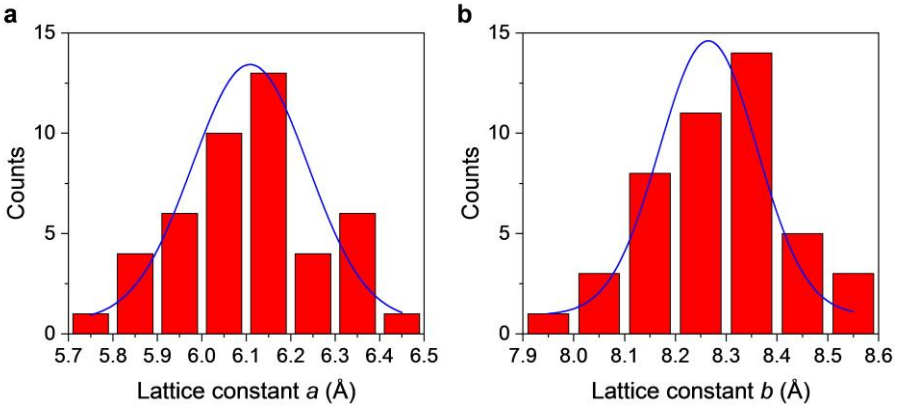


205

206 **Supplementary Figure 12 | a** and **b,** Histograms of lattice constants *a* and *b* acquired

207 from 45 FFT patterns of the C8-BTBT crystal array, respectively.

208

## V. Optical anisotropy analyses of C8-BTBT

The optical absorption process in organic semiconductors is related to the excitation of charge carriers from the highest occupied molecular orbital (HOMO) to the lowest unoccupied molecular orbital (LUMO). According to the Davydov theory[11], the anisotropic optical absorption of herringbone-type organic semiconductor crystals is attributed to the orientation difference of adjacent molecules[12,13]. The resonant interaction between two differently oriented adjacent molecules will lead to the Davydov splitting of molecular terms. The Davydov components can be identified by the dimer energies of exciton states,

$$E_{\pm}^{*} = E_0 + E^{*} + D' \pm I_{12} \tag{S11}$$

where $E_0$ and $E^*$ are the energies of ground and excited states, respectively, $D$' is the Coulomb interaction energy in the excited state, and $I_{12}$ is the resonance interaction energy between the two adjacent molecules. Therefore, the energy exchange between two adjacent molecules will lead to the energy shift and splitting of absorption peaks (Supplementary Fig. 13b). According to the measured absorption peak shift in Fig. 2g, the energy difference caused by polarized absorption can be calculated as:

$$\Delta E = \frac{hc}{\lambda_{90}} - \frac{hc}{\lambda_0} = (6.262\times10^{-34}\ \mathrm{Js})\times(3\times10^{8}\ \mathrm{ms^{-1}})\times\left(\frac{1}{356\times10^{-9}\ \mathrm{m}} - \frac{1}{360\times10^{-9}\ \mathrm{m}}\right)$$

$$= 6.02\times10^{-21}\ \mathrm{J} = 0.04\ \mathrm{eV} \tag{S12}$$

where $\lambda_{90}$ and $\lambda_0$ respectively refer to the wavelengths corresponding to 0° and 90° absorption peaks. Meanwhile, the peak intensity can vary greatly in different polarization states. The polarization dependence of the Davydov components can be determined by the transition dipole moments ($\boldsymbol{\mu}$) from ground to excited states[13]. In a dimer system (two molecules in a crystal lattice), $\boldsymbol{\mu}$ can be expressed as:

$$\boldsymbol{\mu}_{\pm} = \frac{1}{\sqrt{2}}[\langle\Psi_1\Psi_2 \mid q\boldsymbol{r} \mid \Psi_1\Psi_2^{*}\rangle \pm \langle\Psi_1\Psi_2 \mid q\boldsymbol{r} \mid \Psi_1^{*}\Psi_2\rangle] = \frac{1}{\sqrt{2}}(\boldsymbol{\mu}_2 \pm \boldsymbol{\mu}_1) \tag{S13}$$

where $q$ is the elementary charge, $\boldsymbol{r}$ is the net distance of charge displacement, $\Psi$ and $\Psi^*$ respectively represent the wavefunctions of ground and excited states, and the subscripts 1 and 2 refer to the two adjacent herringbone molecules (namely

Molecule 1 and Molecule 2, respectively). The directions of $\boldsymbol{\mu}$ in each molecule are marked by red arrows in Supplementary Fig. 13a according to the density function theory-calculated positions in Supplementary Table 4. For the transition from ground to the first excited state, the angle between $\boldsymbol{\mu}$ and the molecular π plane is ~0.6°. Therefore, the arrangement of the in-plane projections of $\boldsymbol{\mu}$ can be approximated to be the same as that of the herringbone-stacked C8-BTBT molecules. Consequently, we can label $\boldsymbol{\mu}_1$ and $\boldsymbol{\mu}_2$ respectively in two adjacent C8-BTBT molecules of a crystal lattice (Fig. 2f). By simple geometrical addition of vectors, we obtain the projections of $\boldsymbol{\mu}$ along *a* axis ($\boldsymbol{\mu}_a = \boldsymbol{\mu}_2+\boldsymbol{\mu}_1$) and along *b* axis ($\boldsymbol{\mu}_b = \boldsymbol{\mu}_2-\boldsymbol{\mu}_1$). Since the absorption intensity can be described by the oscillator strength (*f*), which is proportional to the dipole strength ($D = |\boldsymbol{\mu}|^2$)[13]. The anisotropic ratio of the peak intensity can be roughly estimated as $1/\tan^2(\alpha/2) = 3.8$ with a herringbone angle $\alpha$ of 54.2°. Note that due to the Davydov shift of the absorption peak, the absorption anisotropic ratio at a fixed wavelength can be larger (*e.g.*, ~5.6 at 365 nm, Supplementary Fig. 14).

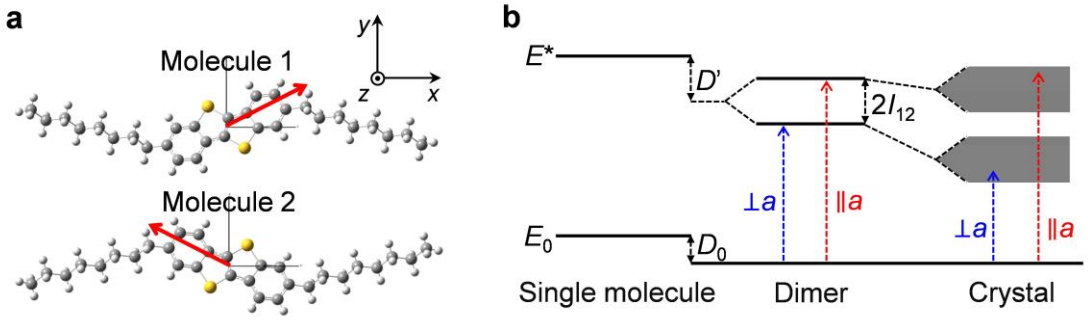


**Supplementary Figure 13 | a,** Projections of $\boldsymbol{\mu}$ (marked in red arrows) in molecular π planes of two adjacent herringbone-stacked C8-BTBT molecules. The calculated positions of $\boldsymbol{\mu}$ are shown in Supplementary Table 4. **b,** Schematic illustration of Davydov splitting in different systems[11].

**Supplementary Table 4** | Calculated components of $\boldsymbol{\mu}$ in orthogonal coordinate, with $x$ and $y$ axes in molecular π plane and z axis normal to molecular π plane. The corresponding dipole strength and oscillator strength are also listed.

| Excited state | $\boldsymbol{\mu}_x$ | $\boldsymbol{\mu}_y$ | $\boldsymbol{\mu}_z$ | $D$ | $f$ |
|---|---|---|---|---|---|
| 1 | ±2.3547 | 1.1661 | -0.0270 | 6.9053 | 0.6199 |
| 2 | ±1.9813 | 0.0321 | 0.2522 | 3.9903 | 0.3865 |
| 3 | ±0.0006 | 0.0000 | 0.0001 | 0.0000 | 0.0000 |

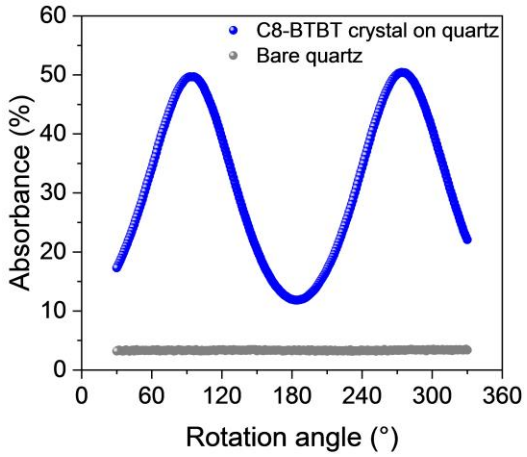


**Supplementary Figure 14** | Angle-resolved absorbance of a C8-BTBT crystal on quartz substrate under 365 nm polarized light. The absorption anisotropic ratio of C8-BTBT is calculated to be ~5.6 according to $(A_{C8,max}-A_{quartz})/(A_{C8,min}-A_{quartz})$, where $A_{C8,max}$ and $A_{C8,min}$ respectively represent the maximum and minimum absorbance of C8-BTBT, and $A_{quartz}$ is the absorbance of the quartz substrate.

## VI. Calculations of the device performance

The hole mobility ($\mu_h$) of the OPT in the saturation regime is calculated by:

$$\mu_h = \frac{2L}{WC_i}\left(\frac{\partial\sqrt{I_{DS}}}{\partial V_G}\right)^2 \quad \text{(S14)}$$

where $L$ and the effective $W$ are respectively 25 μm and 75 μm according to the device structure of the OPT (Supplementary Fig. 15a-c). $C_i$ is $1.2\times10^{-8}$ F cm$^{-2}$ for a 300 nm-thick $SiO_2$ layer[14], and is ~$1.8\times10^{-8}$ F cm$^{-2}$ in our device configuration with ~200 nm-thick $SiO_2$ serving as the gate dielectric. $\mu_h$ is calculated to be 2.6 cm$^2$ V$^{-1}$ s$^{-1}$ according to the slope of the black solid line in Supplementary Fig. 15d.

The figure-of-merit parameters of the OPT are calculated as follows. The photosensitivity is defined as the ratio of the photogenerated current ($I_{ph}$) to the dark current ($I_{dark}$). The responsivity ($R$) of a photodetector is:

$$R = \frac{I_{light} - I_{dark}}{P} = \frac{I_{ph}}{P} \quad \text{(S15)}$$

The specific detectivity ($D^*$) of a photodetector is calculated by:

$$D^* = \frac{R\sqrt{S}}{\sqrt{2qI_d}} \quad \text{(S16)}$$

where $S$ is the effective device area determined by 75×25 μm$^2$ in the channel region of the OPT.

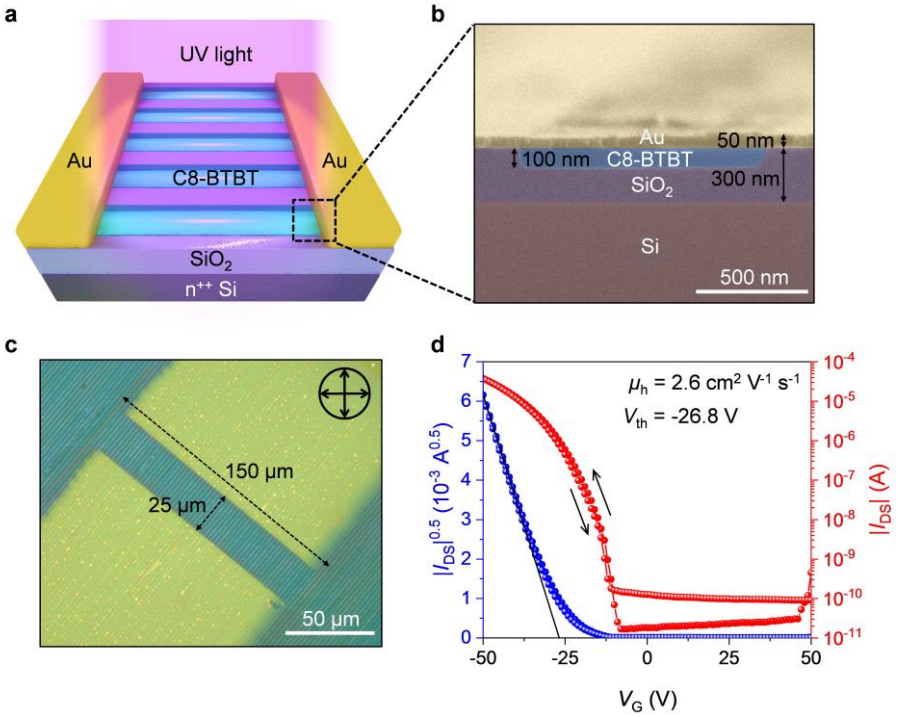


285

286 **Supplementary Figure 15 | a,** Schematic illustration of the bottom-gate top-contact
287 OPT based on C8-BTBT crystal array. **b,** Colored cross-sectional SEM image of the
288 OPT, indicating that ~100 nm-thick $SiO_2$ has been etched away and the remaining 200
289 nm-thick $SiO_2$ underneath the C8-BTBT crystal serves as the gate dielectric. **c,**
290 Cross-polarized optical microscopy image of the OPT. The channel length is 25 μm,
291 while the effective channel width is ~75 μm (half of the measured value) according to
292 the structure of the periodic crystal array. **d,** Double-sweep transfer curves of the OPT
293 in the dark ($V_{DS}$ = -40 V). The black solid line (*i.e.*, tangent line of $\sqrt{I_{DS}}$ *versus* $V_G$
294 curve) is used to extract $V_{th}$ and calculate $\mu_h$.

295

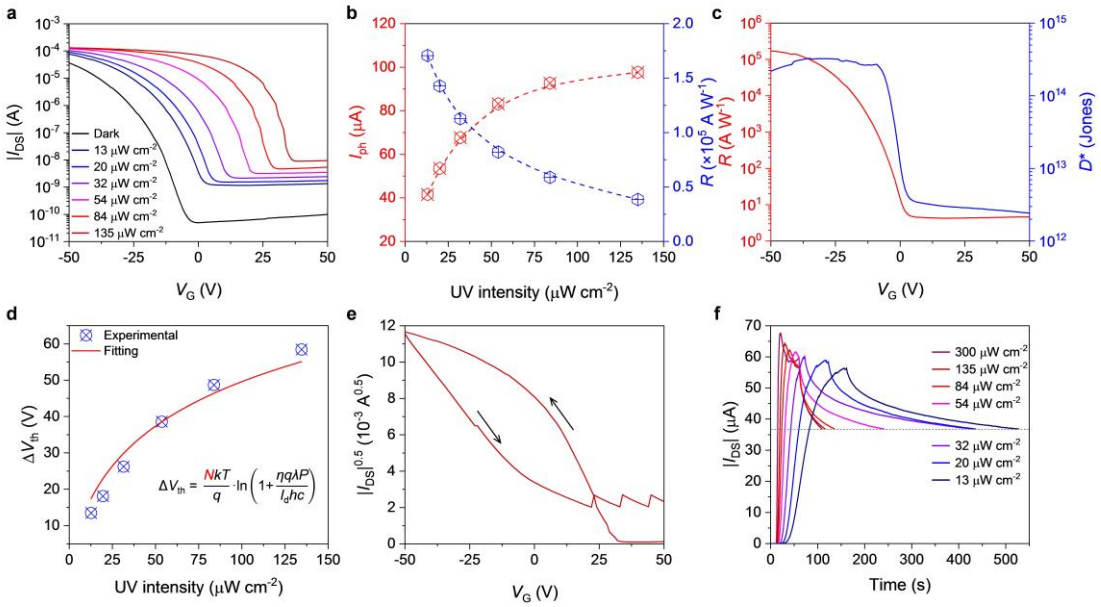


**Supplementary Figure 16 | a,** Transfer characteristics of the OPT in the dark and under the illumination of unpolarized UV light with different intensities ($V_{DS}$ = -40 V). **b,** Dependence of $I_{ph}$ and $R$ on UV intensity. **c,** Dependence of $R$ and $D^*$ on $V_G$ (UV intensity = 13 μW cm$^{-2}$). **d,** Dependence of $\Delta V_{th}$ on UV intensity, the empirical parameter $N$ is fitted to be 775.6 according to the parameters listed in Supplementary Table 2. **e,** Double-sweep transfer curve of the OPT under the illumination of unpolarized UV light with an intensity of 135 μW cm$^{-2}$ ($V_{DS}$ = -40 V). **f,** Time-related evolution of $I_{DS}$ upon turning on/off the unpolarized UV light with different intensities ($V_{DS}$ = -40 V, $V_G$ = 25 V). $I_{DS}$ decays slowly after turnning off the light due to the gradual detrapping process.

## VII. Characterizations of interfacial trap sites on $SiO_2$

To assess the critical role the $SiO_2$/organic semiconductor interface played in charge trapping, bottom-gate top-contact OPTs were fabricated based on different dielectric layers, including bare $SiO_2$, $O_3$-treated $SiO_2$, and $SiO_2$ covered by active group-free divinyltetramethylsiloxane-bis(benzocyclobutene) (BCB) and perfluoro(1-butenyl vinyl ether) polymer (CYTOP) layers. The BCB and CYTOP layers were fabricated by a spin-coating method reported elsewhere[15,16]. 50 nm-thick C8-BTBT film was then thermally deposited on the dielectrics to serve as the active layer, and 50 nm-thick thermally deposited Au electrodes functioned as the source/drain electrodes. The transfer curves of the OPTs based bare $SiO_2$ and $O_3$-treated $SiO_2$ dielectrics exhibit pronounced positive drift under illumination (Supplementary Fig. 17a,b), while the OPTs based on BCB and CYTOP dielectrics exhibit much inferior photoresponse (Supplementary Fig. 17c,d). Since C8-BTBT was thermally deposited simultaneously on the above-mentioned dielectrics to exclude the possible device deviation caused by material growth, and the photoelectric measurements were conducted in a vacuum chamber to exclude the external influence of water/oxygen, we infer that the remaining interfacial active groups on $SiO_2$ surface should be the main source of electron trap sites under illumination.

We further clarify the existence of electron trap sites on $SiO_2$ by scanning kelvin probe force microscopy (SKPM). 50 nm-thick Au electrodes were thermally deposited on different gate dielectrics to function as the source/drain electrodes with heavily n-doped Si ($n^{++}$ Si) serving as the gate. SKPM measurements were conducted by scanning the channel between drain and source electrodes (Supplementary Fig. 18a). During the scan, 10 V bias stress was applied at the gate while the source/drain electrodes were connected to ground, and the time-related potential change between the probe and the scanned surface was recorded. For $SiO_2$ dielectric layer that is susceptible to interfacial active groups such as –OH, a positive gate bias can induce an electrochemical change and lead to the trapping of negative charges (Supplementary Fig. 18b). A possible mechanism can be expressed as $4–OH + O_2 + 4e^- \rightleftharpoons 4–O^- + 2H_2O$ in ambient air or $2–OH + 2e^- \rightleftharpoons 2–O^- + H_2$ when oxygen is not

available[17]. The trapping of negative charges on $SiO_2$ can be evidenced by the rapid potential drop with the increase of scanning time (left of Supplementary Fig. 18c). Further, zero gate bias was applied after scanning the channel with 10 V bias stress for 255 s, a negative potential difference of ~-2.5 V can be observed in the channel region of $SiO_2$ (Supplementary Fig. 19a), indicating the strong capability of negative charge retention on $SiO_2$ surface. In comparison, after passivating the $SiO_2$ surface by active group-free CYTOP dielectric layer, the surface potential remains quite stable with negligible potential drop with scanning time increasing (right of Supplementary Fig. 18c), and the potential quickly recovers to 0 V upon applying zero gate bias (Supplementary Fig. 19b), which confirms that the introduction of CYTOP layer can effectively eliminate the interfacial trap sites.

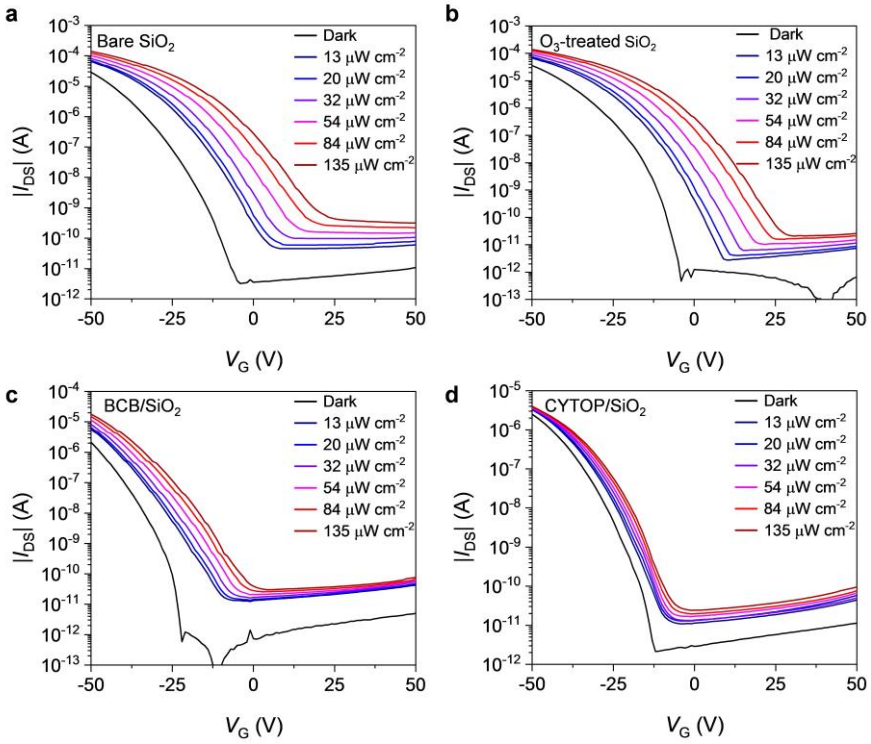


**Supplementary Figure 17 |** Light intensity-dependent transfer characteristics of the OPTs based on the same batch of thermally deposited C8-BTBT films on **a,** bare $SiO_2$ dielectrics, **b,** $O_3$-treated $SiO_2$ dielectrics, and active group-free dielectrics including **c,** BCB and **d,** CYTOP ($V_{DS}$ = -40 V).

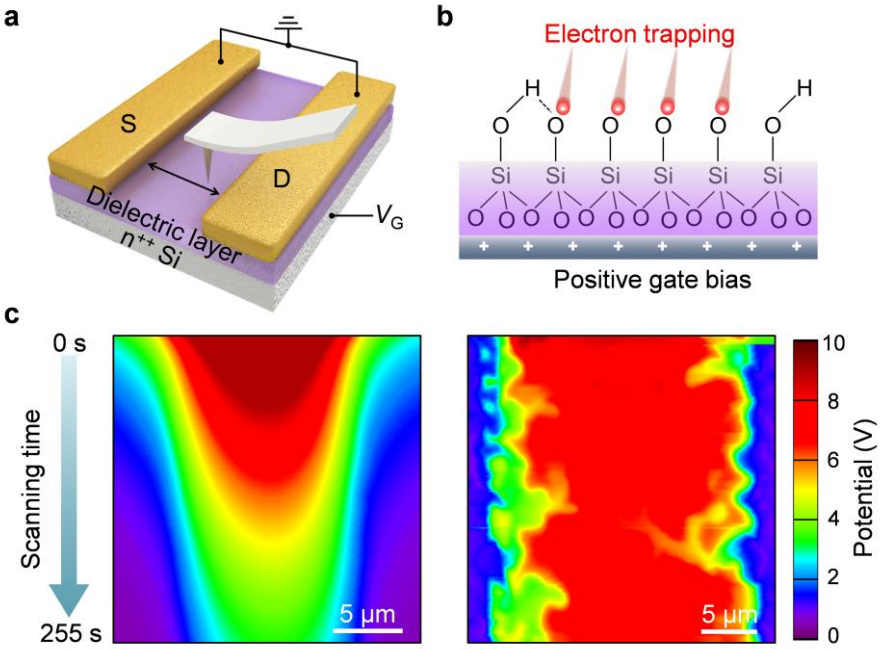


**Supplementary Figure 18 | a,** Schematic illustration of the device configuration for performing SKPM tests. **b,** Schematic illustration of the electron trapping mechanism on $SiO_2$ dielectrics. **c,** Potential mapping of the channel region on $SiO_2$ dielectrics (left) and CYTOP dielectrics (right) under a gate bias of 10 V.

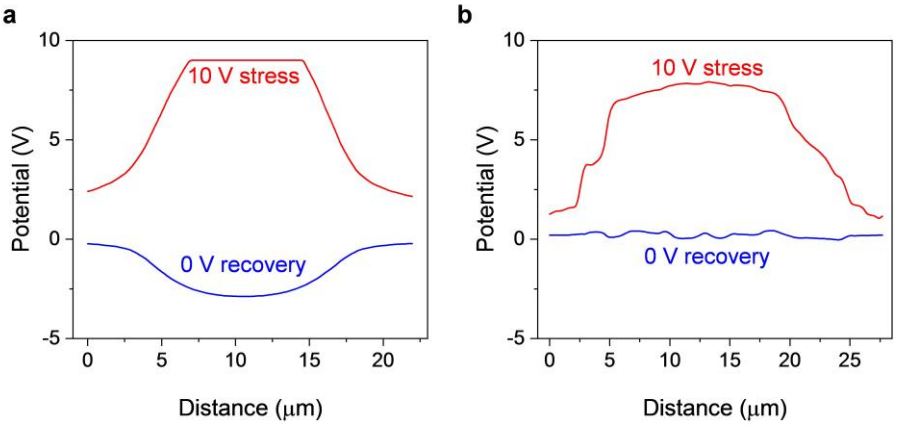


**Supplementary Figure 19 |** Comparison of the potential distributions in the channel regions of the devices on **a,** $SiO_2$ dielectrics and **b,** CYTOP dielectrics measured under a gate bias of 10 V (red curves) and after resetting the gate bias to zero (blue curves).

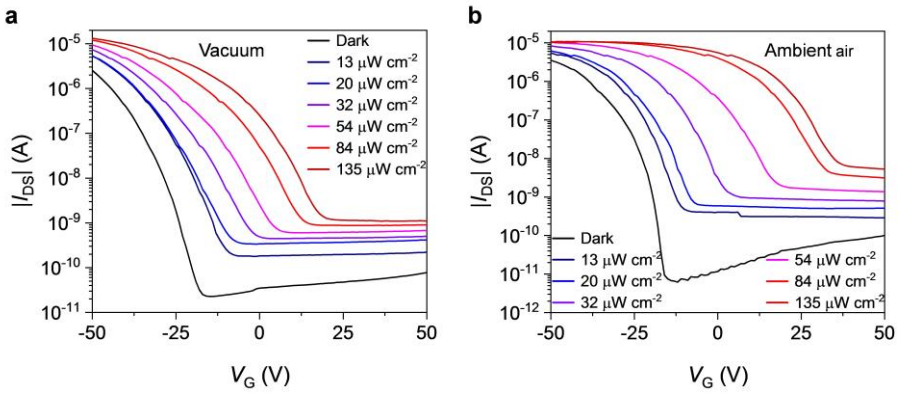


**Supplementary Figure 20** | Light intensity-dependent transfer characteristics of the OPT based on C8-BTBT crystal array on $SiO_2$/Si substrate tested in **a,** vacuum and **b,** ambient air ($V_{DS}$ = -40 V). In both cases the transfer curves exhibit pronounced positive drift under light illumination, indicating the strong electron tapping capability of the OPT. Note that the existence of water/oxygen in ambient air can result in the strong p-type doping effect on organic semiconductors[15,18], thus causing a more positive shift of $V_{th}$. However, water/oxygen can also lead to bias stress instability in OPTs (*i.e.*, drift of transfer curves in the dark)[19]. In order to acquire stable and repeatable photoresponse, we conducted all photoelectric measurements in vacuum unless otherwise mentioned.

## VIII. Analyses of polarization-dependent photoresponse

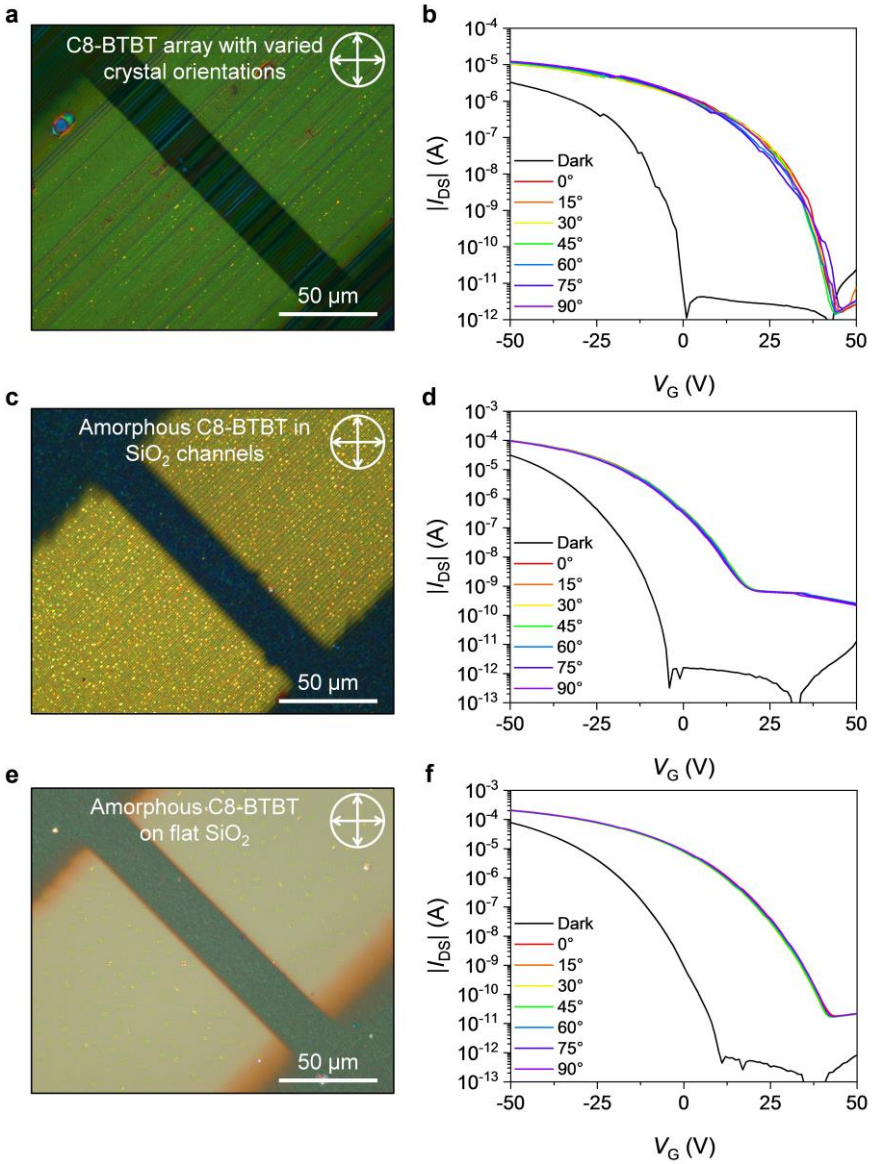


**Supplementary Figure 21 | a,** Cross-polarized optical microscopy image of the OPT based on C8-BTBT array with varied crystal orientations in lyophobic $SiO_2$ channels treated by FTS. **b,** Polarization-dependent transfer curves of the device in (a) ($V_{DS}$ = -40 V). **c,** Cross-polarized optical microscopy image of the OPT based on 50 nm-thick thermally deposited amorphous C8-BTBT in $SiO_2$ channels. **d,** Polarization-dependent transfer curves of the device in (c) ($V_{DS}$ = -40 V). **e,** Cross-polarized optical microscopy image of the OPT based on 50 nm-thick thermally deposited amorphous C8-BTBT on flat $SiO_2$ surface. **f,** Polarization-dependent transfer curves of the device in (e) ($V_{DS}$ = -40 V).

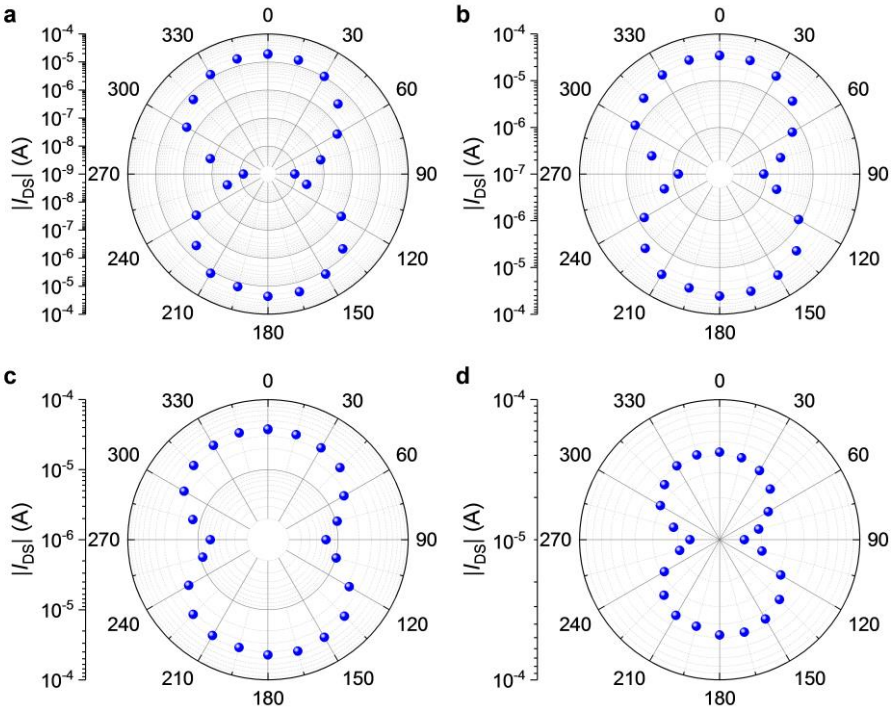


**Supplementary Figure 22 | a-d,** Polarization-dependent variation of $I_{DS}$ at $V_G$ = 20 V, 10 V, 0 V, and -10 V, respectively ($V_{DS}$ = -40 V).

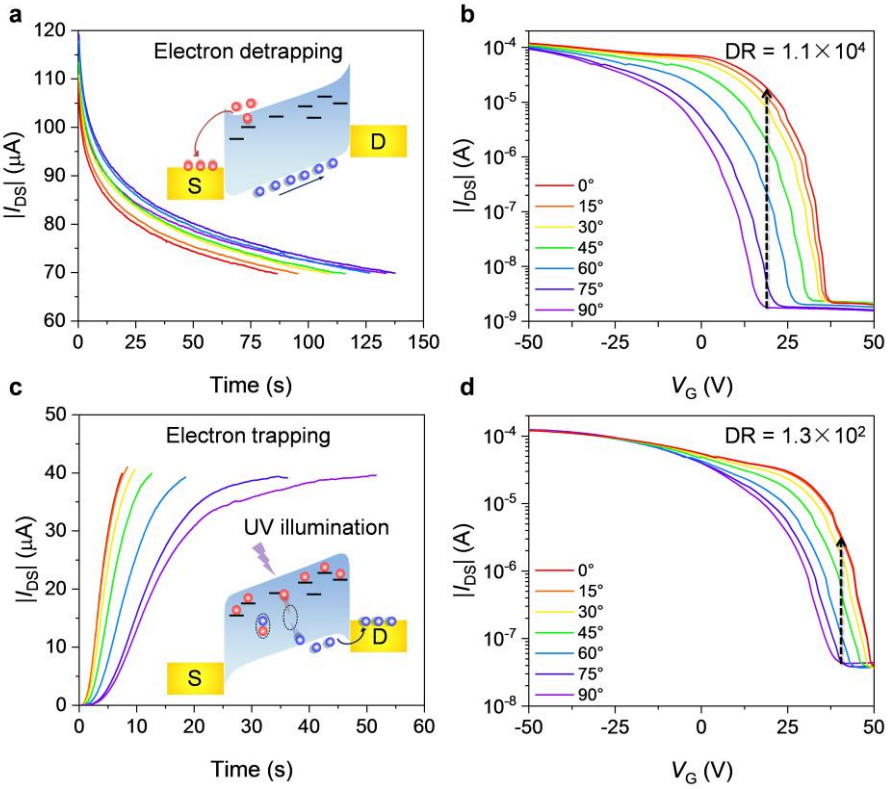


395

396 **Supplementary Figure 23 | a**, Time-related erasing process in the dark to detrap
397 electrons ($V_G$ = -60 V, $V_{DS}$ = -40 V). $I_{DS}$ was reset to the same level to ensure stable
398 and repeatable transfer characteristics in the dark (Supplementary Fig. 25) before the
399 measurement of polarized photoresponse. **b,** Corresponding polarization-dependent
400 transfer curves of the OPT measured after the erasing process in (a). **c,** Time-related
401 programming process under the illumination of polarized UV light to fill trap sites ($V_G$
402 = 25 V, $V_{DS}$ = -40 V). **d,** Corresponding polarization-dependent transfer curves of the
403 OPT measured after the programming process in (c).

404

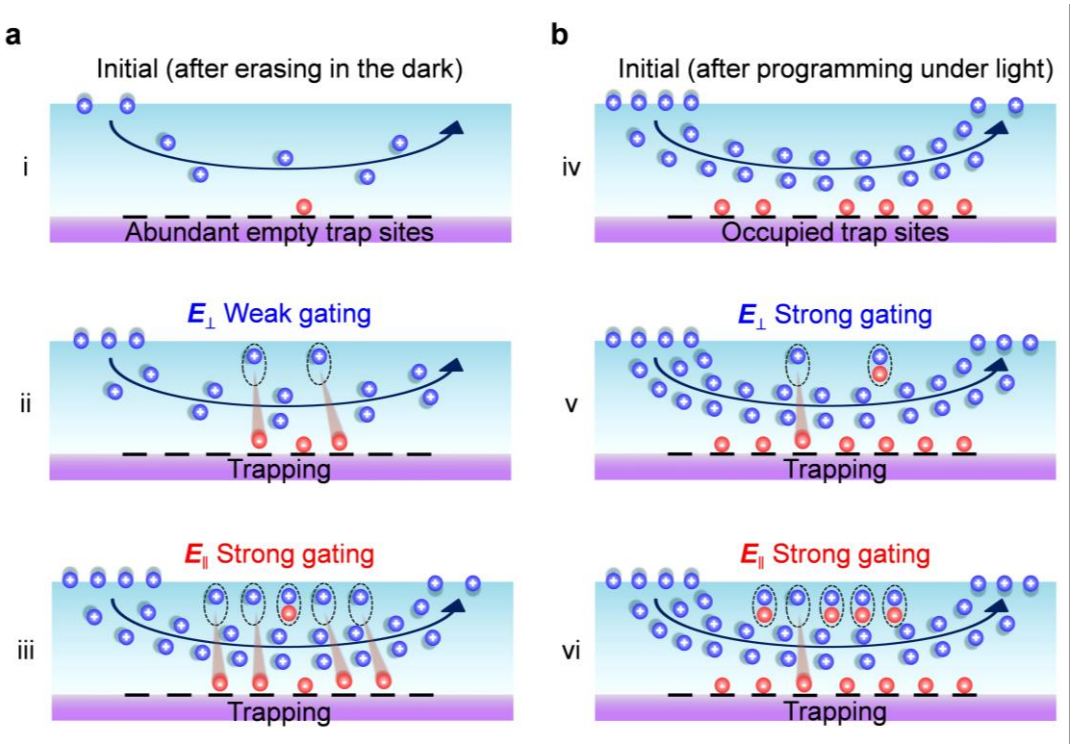


405

406 **Supplementary Figure 24 |** Schematic illustrations of the anisotropic charge trapping

407 mechanisms of the OPT after **a,** erasing in the dark and **b,** programming under light

408 illumination.

409

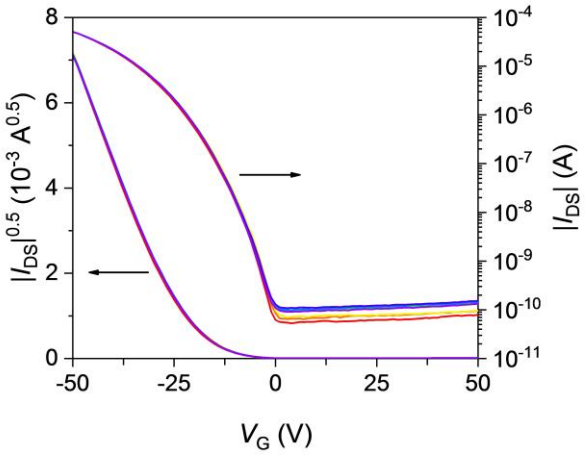


410

411 **Supplementary Figure 25 |** Transfer curves of the OPT after erasing in the dark ($V_G$

412 = -60 V, $V_{DS}$ = -40 V), which are highly repeatable with negligible $V_{th}$ shift.

413

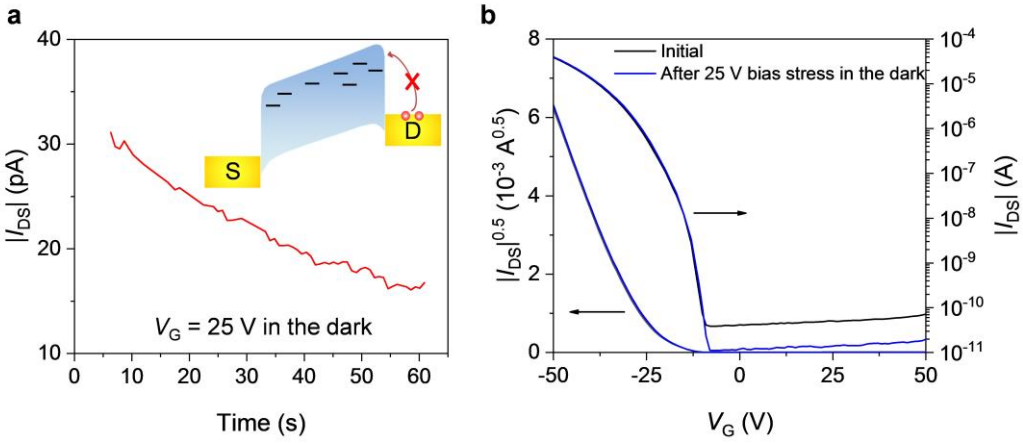


414

415 **Supplementary Figure 26 | a,** Time-related programming process in the dark ($V_G$ =

416 25 V, $V_{DS}$ = -40 V). The inset illustration depicts that no additional electron injection

417 occurs under a continuous gate bias of 25 V in the dark. **b,** Transfer curves of the OPT

418 in the dark before (black curve) and after (blue curve) 25 V bias stress in (a), showing

419 negligible $V_{th}$ shift. The minority charge carrier injection phenomenon has been

420 observed in small-bandgap organic semiconductors or those with thermally damaged

421 electrode/active layer interfaces[20]. Injection of electrons from electrodes can lead to

422 positive drift of the transfer curve and increasing $I_{DS}$ under a continuous positive gate

423 bias. Thanks to the relatively large bandgap of C8-BTBT and the careful tuning of Au

424 deposition rate, the OPT exhibits remarkable bias stress stability in the dark.

425

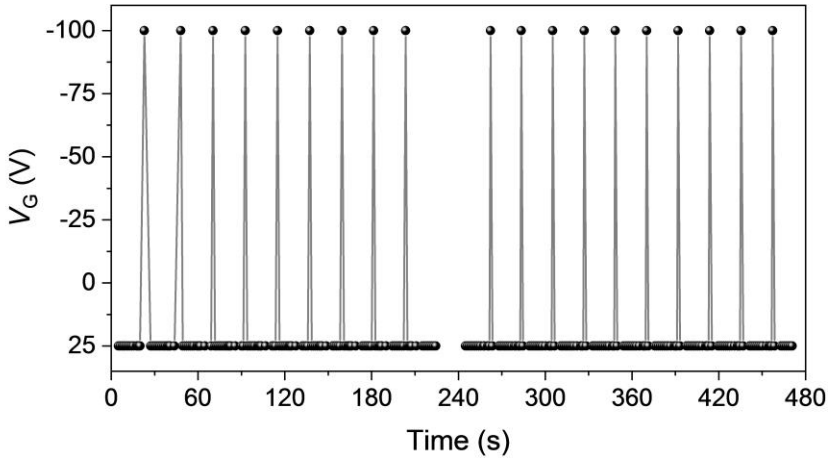


**Supplementary Figure 27 |** Applied time-dependent $V_G$ corresponding to Fig. 3f ($V_{DS}$ = -40 V). Polarized photoresponse of the OPT was obtained at a continuous $V_G$ of 25 V, and an erasing gate bias ($V_G$ = -100 V) was applied to reset the OPT in the dark. The interval between two erasing $V_G$ is ~22 s.

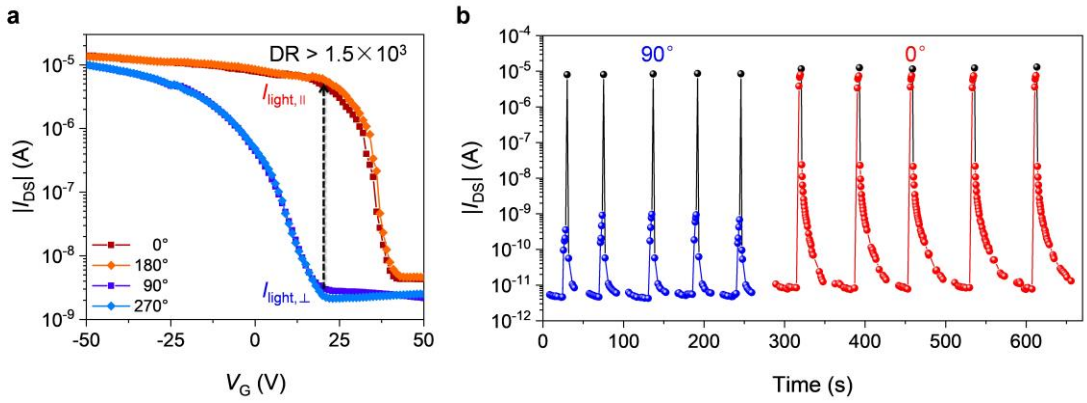


**Supplementary Figure 28 | a,** Polarization-dependent transfer curves and **b,** transient photoresponse of the OPT after preservation in ambient air for 6 months ($V_{DS}$ = -40 V).

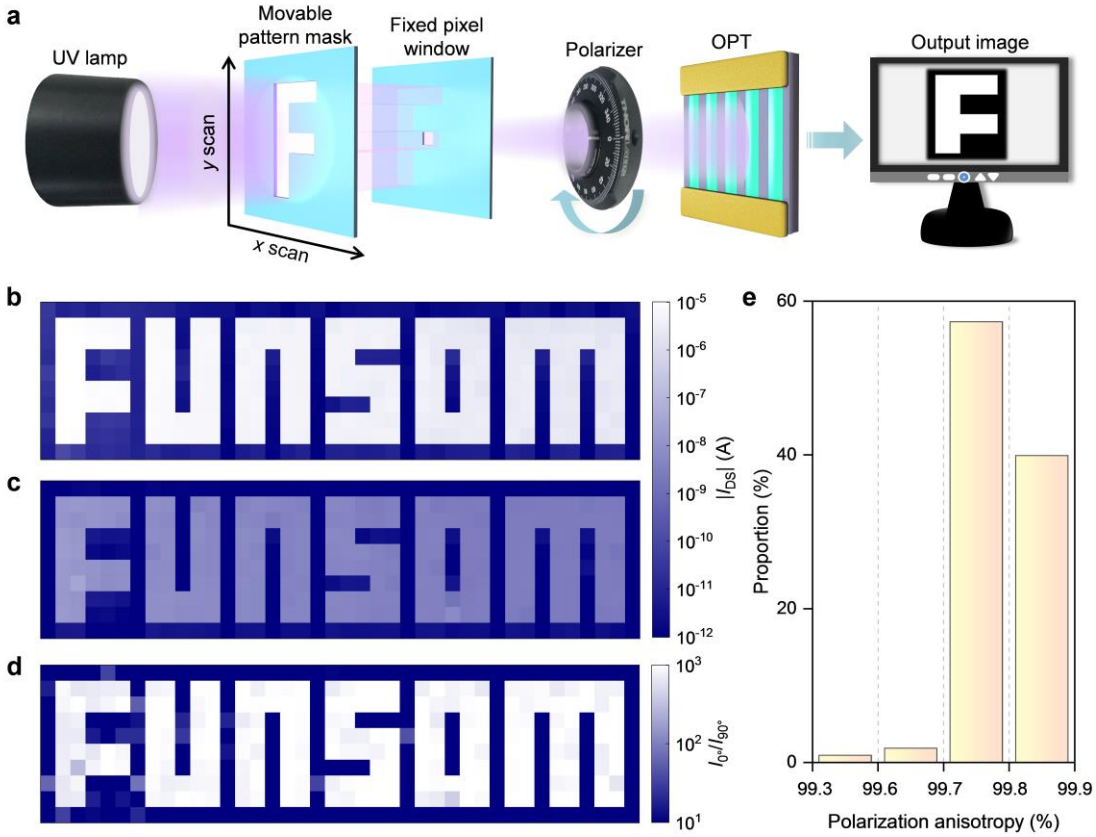


**Supplementary Figure 29 | a,** Schematic illustration of the experiment setup for single-device polarization imaging. Light signals passing through the pattern mask first shone through a fixed pixel window (4×4 $mm^2$) and were then collected stepwise by the OPT, and the light polarization state was controlled by a polarizer. **b,** 0° and **c,** 90° polarization imaging of the "FUNSOM" pattern containing 40×10 imaging pixels, respectively. The data of each pixel was acquired from the time-dependent $I_{DS}$ at 5 s after illumination ($V_G$ = 25 V, $V_{DS}$ = -40 V). **d,** Imaging of the 0° to 90° photocurrent ratio ($I_0/I_{90}$) of the "FUNSOM" pattern containing 40×10 imaging pixels. **e,** Histogram of the polarization anisotropy within the effective projection region of the "FUNSOM" pattern.

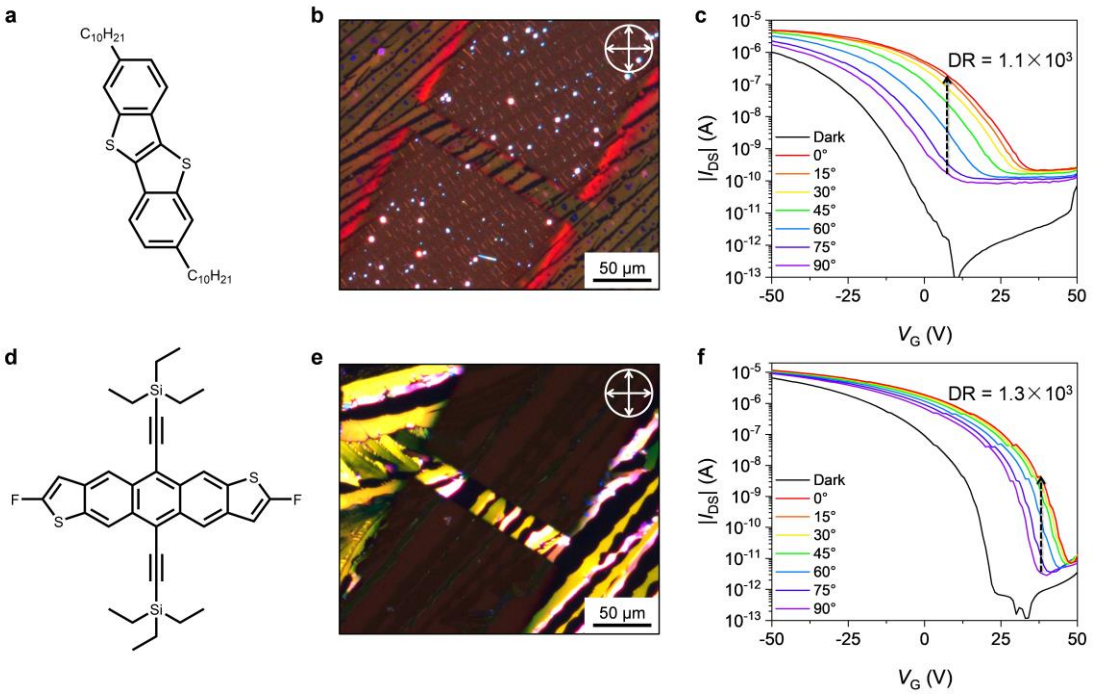


**Supplementary Figure 30 | a,** Molecular structure of C10-BTBT. **b,** Cross-polarized optical microscopy image of solution-grown C10-BTBT microribbons on $SiO_2$/Si substrate. **c,** Polarization-dependent transfer curves of the OPT based on C10-BTBT microribbons under 365 nm polarized light with an intensity of 110 μW $cm^{-2}$ ($V_{DS}$ = -40 V). The maximum photoresponse direction is set as the 0° reference. **d,** Molecular structure of dif-TES ADT. **e,** Cross-polarized optical microscopy image of solution-grown dif-TES ADT microribbons on $SiO_2$/Si substrate. **f,** Polarization-dependent transfer curves of the OPT based on dif-TES ADT microribbons under 525 nm polarized light with an intensity of 10 μW $cm^{-2}$ ($V_{DS}$ = -40 V). The maximum photoresponse direction is set as the 0° reference. Both C10-BTBT and dif-TES ADT microribbons were fabricated by a blade-coating method reported elsewhere[21].

**Supplementary Table 5** | Performance comparison of our PDPG effect-enhanced phototransistors with other state-of-the-art polarization-sensitive photodetectors.

| Material | $\lambda$ (nm) | DR | Ref. |
|---|---|---|---|
| **C8-BTBT crystal array** | **365** | **> 12,000** | **This work** |
| C10-BTBT microbelts | 365 | ~1,100 | This work |
| dif-TES ADT microbelts | 525 | ~1,300 | This work |
| CdSe NWs | 488 | 1.3 | [22] |
| Si NW | 900 | ~2.48 | [23] |
| Carbon nanotubes | 650-1100 | 6.14 | [24] |
| InP NW | 514 | 49 | [25] |
| GeSe flake | 400-950 | 2.16 | [5] |
| $TiS_3$ nanoribbon | 532-808 | 4 | [26] |
| GeAs flake | 400-2000 | 4.4 | [27] |
| $WTe_2$ flake | 514 | 4.9 | [28] |
| α-$MoO_3$ crystal | 254 | 5.2 | [29] |
| $Sb_2Se_3$ nanosheet | 633 | 16 | [30] |
| $CH_3NH_3PbI_3$ NWs | 400-750 | 1.3 | [31] |
| $CsPbBr_3$ NW array | 470 | 2.6 | [8] |
| $(BA)_2PbI_4$ NWs | 492 | 3.62 | [32] |
| $(allyammonium)_2(ethylammonium)_2Pb_3Br_{10}$ | 405 | 15 | [33] |
| $SbI_3/Sb_2O_3$ | 360-532 | 3.14 | [34] |
| $TiS_3$/Si | 405-1050 | 4.6 | [35] |
| BP/$WSe_2$ | 637-1550 | 5.9 | [36] |
| $PdSe_2/FA_{1-x}Cs_xPbI_3$ | 200-1550 | 6.04 | [37] |
| BP/plasmonic Au | 1550 | 8.7 | [38] |
| BP/InSe | 455-950 | 10.8 | [39] |
| $PdSe_2$/Si NWs | 200-4600 | 75 | [40] |
| BP/$MoS_2$ | 2500-3500 | ~100 | [41] |
| Graphene/$PdSe_2$/Ge | 265-3043 | 112.2 | [42] |
| PBnDT-FTAZ:P(NDI2OD-T2) | 350-800 | 1.4 | [43] |
| Pt-complex (1o) | 532 | 2 | [44] |
| DPA microsheet | 450 | 1.9 | [10] |

## IX. Theoretical estimation of partially polarized light detection

Conventionally, polarization navigation sensors require polarizers integrated with polarization-insensitive photodetectors for the detection of partially polarized skylight. To evaluate their detection ability, we now consider a simplified case where the partially polarized incident light is composed of two orthogonally polarized parts, and the light intensities along these two directions are respectively denoted as $I_{\mathrm{pol},\parallel}$ and $I_{\mathrm{pol},\perp}$. The degree of polarization (DoP) of the incident light is thus $(I_{\mathrm{pol},\parallel}-I_{\mathrm{pol},\perp})/(I_{\mathrm{pol},\parallel}+I_{\mathrm{pol},\perp})$. For a linear polarizer, we define that the light transmittance along its optical axis is $T_{\parallel}$, and perpendicular to the optical axis is $T_{\perp}$, its extinction ratio (ER) is thus $T_{\parallel}/T_{\perp}$. If the partially polarized light passes through the polarizer (Supplementary Fig. 31a), the finally measured DR by a polarization-insensitive photodetector should be limited by the ratio of transmitted light intensity:

$$\mathrm{DR} \le (I_{\mathrm{pol},\parallel}T_{\parallel} + I_{\mathrm{pol},\perp}T_{\perp}) / (I_{\mathrm{pol},\parallel}T_{\perp} + I_{\mathrm{pol},\perp}T_{\parallel}) = \left(\frac{1+\mathrm{DoP}}{1-\mathrm{DoP}} \cdot \mathrm{ER}+1\right)/\left(\frac{1+\mathrm{DoP}}{1-\mathrm{DoP}} + \mathrm{ER}\right) \quad \text{(S17)}$$

In practical measurements, the DoP of skylight is only about 60% (or even lower than 30% in UV spectral range)[45], which results in $I_{\mathrm{pol},\parallel}/I_{\mathrm{pol},\perp}$ of only ~4 (or ~1.9 in UV spectral range). Therefore, the increase of ER is favorable for more sensitive detection of partially polarized light (Supplementary Fig. 31b), while a small ER will lead to a degraded DR (Supplementary Fig. 31c) or even indistinguishable signals when DoP is quite small. Although the emerging anisotropic photoactive materials have provided new opportunities for on-chip polarizer-free polarimeters, their application in partially polarized light detection remains unexplored due to the low polarization sensitivity (DR < 10).

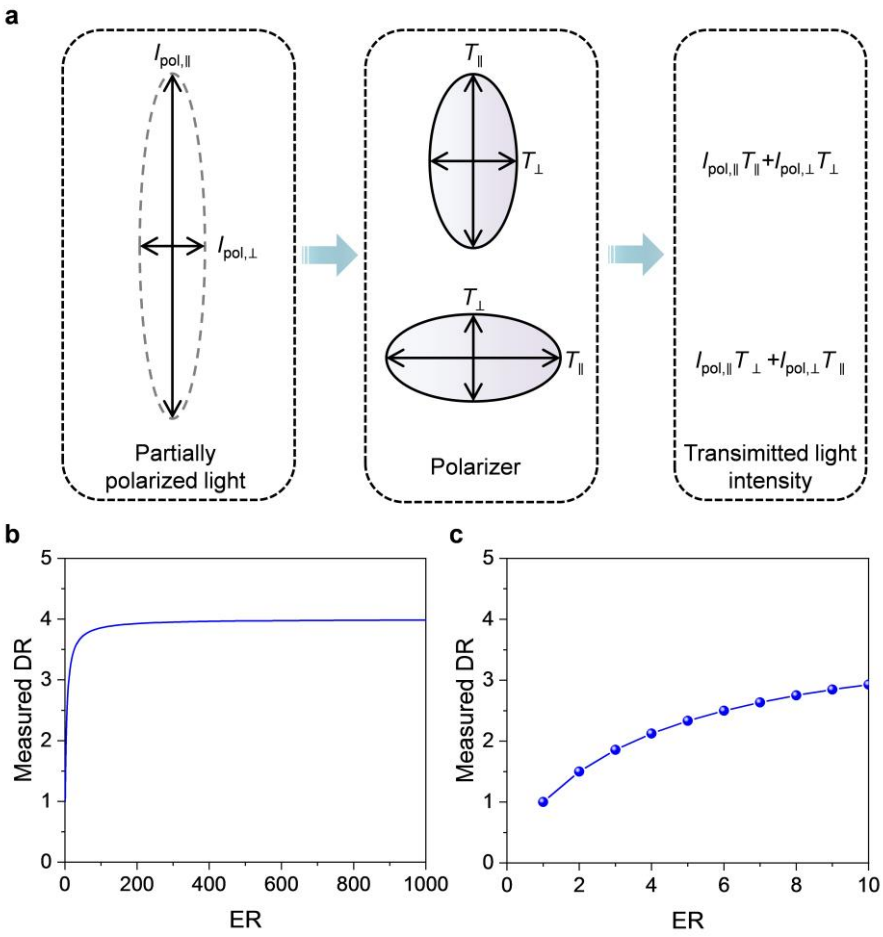


487

488 **Supplementary Figure 31 | a,** Schematics of the detection of partially polarized light.
489 **b,** Predicted relationship between ER of a polarizer and the finally measured DR
490 under a partially polarized light with a DoP of 60%. **c,** Enlarged plot of (b) with ER in
491 a range of 1-10.

492

## X. Polarization navigation measurements

According to the single-scattering Rayleigh model[46], the polarization mode of ideal skylight is symmetrical about the solar meridian (SM), and the e-vector (***E***) of skylight at zenith remains steadily perpendicular to the SM despite the change of time and location, which forms the basis of polarization navigation. By measuring the direction of ***E*** relative to the heading direction, one can deduce the exact orientation relative to the north. Particularly, although the DoP in UV spectral region is relatively low, it maintains most reliable under complex weather conditions compared with that of visible light, which makes UV light advantageous for polarization navigation[47].

During polarization navigation measurements, the crystallographic *a* axis of C8-BTBT crystal array was first aligned towards the north direction with the aid of a compass, and this direction was set as the 0° reference direction. Angle-resolved $I_{DS}$ was then collected stepwise by rotating the OPT clockwise in 15° increments. To eliminate the influence of light intensity change caused by the westward movement of the sun for a better fitting, we set two base lines (namely base line 1 and base line 2) according to the valleys and peaks of the sinusoidal curve, respectively (Supplementary Fig. 33a,c). The normalized $I_{DS}$ is obtained after the subtraction of base line 1 by $(I_{DS}-I_{\text{base line 1}})/(I_{\text{base line 2}}-I_{\text{base line 1}})$, where $I_{\text{base line 1}}$ and $I_{\text{base line 2}}$ represent the current at base line 1 and base line 2, respectively. (Supplementary Fig. 33b,d). The normalized polarization-dependent $I_{DS}$ is fitted by:

$$I_{DS}(\theta) = I_{\parallel}\cos^2(\theta+\varphi)+I_{\perp}\sin^2(\theta+\varphi) \quad \text{(S18)}$$

where $I_{\parallel}$ and $I_{\perp}$ respectively refer to the drain current along and perpendicular to the strongest photoresponse direction, $\theta$ is the angle with respect to the 0° reference direction, and $\varphi$ is the angle between the 0° reference direction and the strongest photoresponse direction. The fitted strongest photoresponse directions are marked by red arrows in polar coordinates (Supplementary Fig. 34a,c), which are ~-14° and ~-16° relative to the 0° reference direction (compass-pointed north), respectively. We then look for the real-time $\Phi_S$ to determine the theoretical orientations of ***E*** at zenith. The location of the measurements is in Suzhou Industrial Park, China (120.7°E, 31.3°N), the measuring time period is 3:42-4:17 p.m., 23/09/2021 and 3:27-4:07 p.m.,

24/09/2021 corresponding to Fig. 5h,k, respectively. Therefore, $\Phi_s$ is in a range of 252° to 257° and 249° to 255°, respectively. The theoretical orientations of $\boldsymbol{E}$ at zenith are thus -18° to -13° and -21° to -15° relative to the north (marked by red arrows in Supplementary Fig. 34b,d). Therefore, both the navigated directions of $\boldsymbol{E}$ (~-14° and ~-16° relative to the compass-pointed north) are located right in the range of the real-time theoretical values, indicating the high accuracy of our novel celestial compass. More polarization navigation measurements at different times and in different weather conditions are presented in Supplementary Fig. 35 and Supplementary Table 6.

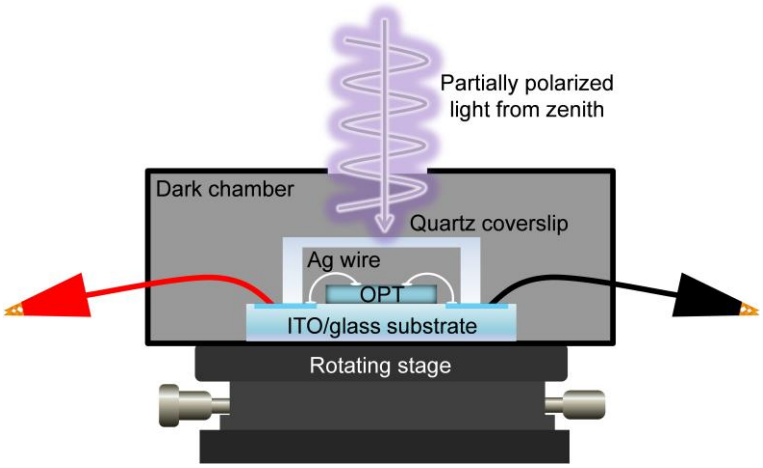


**Supplementary Figure 32 |** Schematic illustration of the experimental setup for polarization navigation measurements. The OPT was fixed into a dark chamber with a drilled circular window (~1.3 cm in diameter) located right above the device area to receive skylight at zenith and exclude light from the surrounding environment.

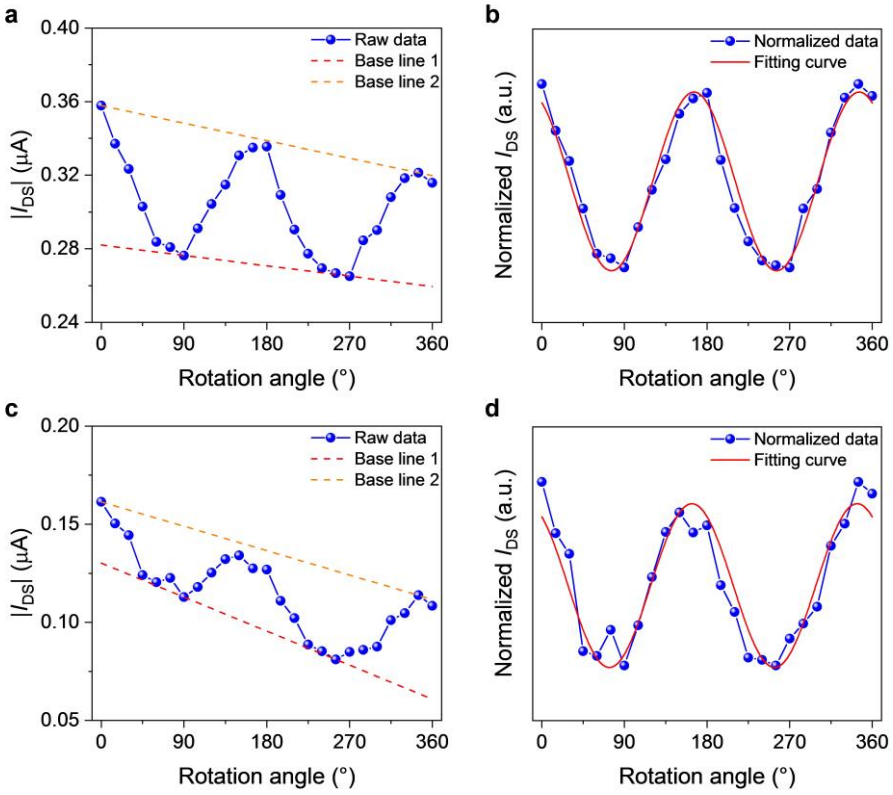


**Supplementary Figure 33 | a,** Polarization-dependent $I_{DS}$ measured under clear skylight during a time period of 3:42-4:17 p.m., 23/09/2021 ($V_G$ = -10 V, $V_{DS}$ = -40 V). **b,** Normalized polarization-dependent $I_{DS}$ (blue curve) and the corresponding fitting curve (red curve) after base line subtraction in (a). **c,** Polarization-dependent $I_{DS}$ measured under cloudy skylight during a time period of 3:27-4:07 p.m., 24/09/2021 ($V_G$ = -10 V, $V_{DS}$ = -40 V). **d,** Normalized polarization-dependent $I_{DS}$ (blue curve) and the corresponding fitting curve (red curve) after base line subtraction in (c).

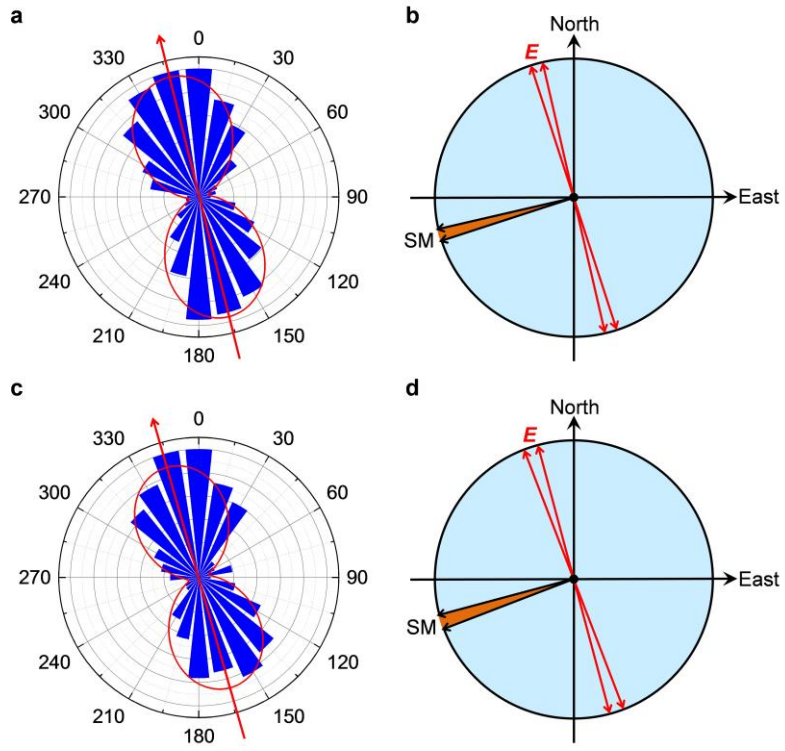


**Supplementary Figure 34 | a,** Polar coordinate plot of normalized polarization-dependent $I_{DS}$ measured under clear sky at 3:42-4:17 p.m. (23/09/2021). The angle between the 0° reference direction and the fitted strongest photoresponse direction is ~-14°. **b,** Corresponding real-time orientations of SM and ***E*** at zenith. $\Phi_s$ is in a range of 252° to 257°, resulting in an ***E*** direction of -18° to -13° relative to the north direction. **c,** Polar coordinate plot of normalized polarization-dependent $I_{DS}$ measured under cloudy sky at 3:27-4:07 p.m. (24/09/2021). The angle between the 0° reference direction and the fitted strongest photoresponse direction is ~-16°. **d,** Corresponding real-time orientations of SM and ***E*** at zenith. $\Phi_s$ is in a range of 249° to 255°, resulting in an ***E*** direction of -21° to -15° relative to the north direction.

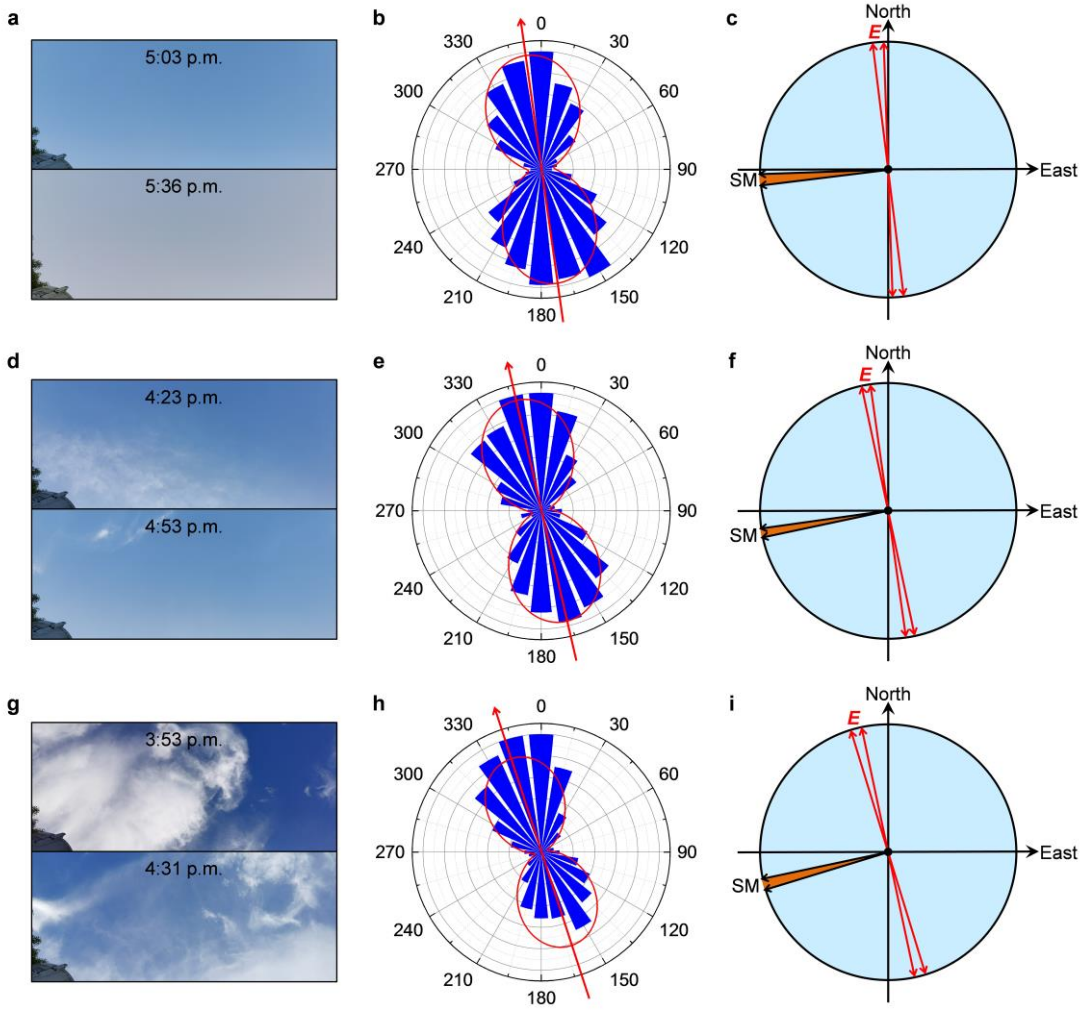


**Supplementary Figure 35 | a,** Real-time photograph of the clear sky at 5:03-5:36 p.m. (23/09/2021). **b,** Corresponding polar coordinate plot of normalized polarization-dependent $I_{DS}$. The angle between the 0° reference direction and the fitted strongest photoresponse direction is ~-8°. **c,** Corresponding real-time orientations of SM and ***E*** at zenith. $\Phi_s$ is in a range of 263° to 268°, resulting in an ***E*** direction of -7° to -2° relative to the north direction. **d,** Real-time photograph of the cloudy sky at 4:23-4:53 p.m. (24/09/2021). **e,** Corresponding polar coordinate plot of normalized polarization-dependent $I_{DS}$. The angle between the 0° reference direction and the fitted strongest photoresponse direction is ~-13°. **f,** Corresponding real-time orientations of SM and ***E*** at zenith. $\Phi_s$ is in a range of 258° to 262°, resulting in an ***E*** direction of -12° to -8° relative to the north direction. **g,** Real-time photograph of the cloudy sky at 3:53-4:31 p.m. (25/09/2021). **h,** Corresponding polar coordinate plot of normalized polarization-dependent $I_{DS}$. The angle between the 0° reference direction and the fitted

strongest photoresponse direction is ~-18°. **i,** Corresponding real-time orientations of SM and ***E*** at zenith. $\Phi_s$ is in a range of 253° to 258°, resulting in an ***E*** direction of -17° to -12° relative to the north direction.

**Supplementary Table 6** | Summary of polarization navigation measurements conducted at different times and in different weather conditions.

| Weather condition | Time | Date | Real-time $\Phi_s$ | Real-time ***E*** relative to the north | Navigated ***E*** relative to the 0° reference |
|---|---|---|---|---|---|
| Cloudy | 3:27-4.07 p.m. | 24/09/2021 | 249° to 255° | -21° to -15° | -16° |
| Clear | 3:42-4:17 p.m. | 23/09/2021 | 252° to 257° | -18° to -13° | -14° |
| Cloudy | 3:53-4:31 p.m. | 25/09/2021 | 253° to 258° | -17° to -12° | -18° |
| Cloudy | 4:23-4:53 p.m. | 24/09/2021 | 258° to 262° | -12° to -8° | -13° |
| Clear | 5:03-5:36 p.m. | 23/09/2021 | 263° to 268° | -7° to -2° | -8° |

## XI. References


1. Kim CH, et al. A compact model for organic field-effect transistors with improved output asymptotic behaviors. *IEEE Trans. Electron Devices* **60**, 1136-1141 (2013).
2. Fayez M, Morsi KM, Sabry MN. OTFTs compact models: analysis, comparison, and insights. *IET Circ. Device Syst.* **11**, 409-420 (2017).
3. Baeg KJ, Binda M, Natali D, Caironi M, Noh YY. Organic light detectors: photodiodes and phototransistors. *Adv. Mater.* **25**, 4267-4295 (2013).
4. Fang H, Hu W. Photogating in low dimensional photodetectors. *Adv. Sci.* **4**, 1700323 (2017).
5. Wang X, et al. Short-wave near-infrared linear dichroism of two-dimensional germanium selenide. *J. Am. Chem. Soc.* **139**, 14976-14982 (2017).
6. Tong L, et al. Stable mid-infrared polarization imaging based on quasi-2D tellurium at room temperature. *Nat. Commun.* **11**, 2308 (2020).
7. Feng X, et al. 2D inorganic bimolecular crystals with strong in-plane anisotropy for second-order nonlinear optics. *Adv. Mater.* **32**, 2003146 (2020).
8. Feng J, et al. Crystallographically aligned perovskite structures for high-performance polarization-sensitive photodetectors. *Adv. Mater.* **29**, 1605993 (2017).
9. Li L, et al. Two-dimensional hybrid perovskite-type ferroelectric for highly polarization-sensitive shortwave photodetection. *J. Am. Chem. Soc.* **141**, 2623-2629 (2019).
10. Wang T, et al. Intrinsic linear dichroism of organic single crystals toward high-performance polarization-sensitive photodetectors. *Adv. Mater.*, 2105665 (2021).
11. Schwoerer M, Wolf HC. *Organic Molecular Solids Ch. 6* (Wiley-VCH, 2007).
12. Arai S, et al. Layered-herringbone polymorphs and alkyl-chain ordering in molecular bilayer organic semiconductors. *Adv. Funct. Mater.* **30**, 1906406 (2019).
13. Meyenburg I, et al. Temperature-resolved optical spectroscopy of pentacene polymorphs: variation of herringbone angles in single-crystals and interface-controlled thin films. *Phys. Chem. Chem. Phys.* **18**, 3825-3831 (2016).
14. Cao M, et al. Enhanced photoelectrical response of thermodynamically epitaxial organic crystals at the two-dimensional limit. *Nat. Commun.* **10**, 756 (2019).
15. Wu X, et al. Air effect on the ideality of p-type organic field-effect transistors: a double-edged sword. *Adv. Funct. Mater.* **29**, 1906653 (2019).
16. Huang Y, et al. Effectively modulating thermal activated charge transport in organic semiconductors by precise potential barrier engineering. *Nat. Commun.* **12**, 21 (2021).
17. Un HI, et al. Charge-trapping-induced non-ideal behaviors in organic field-effect transistors. *Adv. Mater.* **30**, 1800017 (2018).
18. Jia R, et al. Unraveling the Mechanism of the Persistent Photoconductivity in Organic Phototransistors. *Adv. Funct. Mater.* **29**, 1905657 (2019).
19. Iqbal HF, et al. Suppressing bias stress degradation in high performance solution processed organic transistors operating in air. *Nat. Commun.* **12**, 2352 (2021).
20. Wu X, et al. Improving ideality of p-type organic field-effect transistors via

preventing undesired minority carrier injection. *Adv. Funct. Mater.* **31**, 2100202 (2021).
21. Zhang X, et al. Fast deposition of an ultrathin, highly crystalline organic semiconductor film for high-performance transistors. *Nanoscale Horiz.* **5**, 1096-1105 (2020).
22. Singh A, et al. Polarization-sensitive nanowire photodetectors based on solution-synthesized CdSe quantum-wire solids. *Nano Lett.* **7**, 2999-3006 (2007).
23. Das K, Mukherjee S, Manna S, Ray SK, Raychaudhuri AK. Single Si nanowire (diameter </= 100 nm) based polarization sensitive near-infrared photodetector with ultra-high responsivity. *Nanoscale* **6**, 11232-11239 (2014).
24. Barkelid M, Steele GA, Zwiller V. Probing optical transitions in individual carbon nanotubes using polarized photocurrent spectroscopy. *Nano Lett.* **12**, 5649-5653 (2012).
25. Wang J, Gudiksen MS, Duan X, Cui Y, Lieber CM. Highly polarized photoluminescence and photodetection from single indium phosphide nanowires. *Science* **293**, 1455-1457 (2001).
26. Liu S, et al. Highly polarization sensitive photodetectors based on quasi-1D titanium trisulfide ($TiS_3$). *Nanotechnology* **29**, 184002 (2018).
27. Zhou Z, et al. Perpendicular optical reversal of the linear dichroism and polarized photodetection in 2D GeAs. *ACS Nano* **12**, 12416-12423 (2018).
28. Zhou W, et al. Anomalous and polarization-sensitive photoresponse of Td-$WTe_2$ from visible to infrared light. *Adv. Mater.* **31**, 1804629 (2019).
29. Zhong M, et al. Highly anisotropic solar-blind UV photodetector based on large-size two-dimensional α-$MoO_3$ atomic crystals. *2D Mater.* **5**, 035033 (2018).
30. Song H, et al. Highly anisotropic $Sb_2Se_3$ nanosheets: gentle exfoliation from the bulk precursors possessing 1D crystal structure. *Adv. Mater.* **29**, 1700441 (2017).
31. Gao L, et al. Passivated single-crystalline $CH_3NH_3PbI_3$ nanowire photodetector with high detectivity and polarization sensitivity. *Nano Lett.* **16**, 7446-7454 (2016).
32. Ghoshal D, et al. Catalyst-free and morphology-controlled growth of 2D perovskite nanowires for polarized light detection. *Adv. Opt. Mater.* **7**, 1900039 (2019).
33. Peng Y, et al. Exploiting the bulk photovoltaic effect in a 2D trilayered hybrid ferroelectric for highly sensitive polarized light detection. *Angew. Chem. Int. Ed.* **59**, 3933-3937 (2020).
34. Xiao M, et al. Symmetry-reduction enhanced polarization-sensitive photodetection in core-shell $SbI_3/Sb_2O_3$ van der Waals heterostructure. *Small* **16**, 1907172 (2020).
35. Niu Y, et al. Polarization-sensitive and broadband photodetection based on a mixed-dimensionality $TiS_3$/Si p-n junction. *Adv. Opt. Mater.* **6**, 1800351 (2018).
36. Ye L, et al. Highly polarization sensitive infrared photodetector based on black phosphorus-on-$WSe_2$ photogate vertical heterostructure. *Nano Energy* **37**, 53-60 (2017).
37. Zeng LH, et al. Multilayered $PdSe_2$/perovskite Schottky junction for fast, self-powered, polarization-sensitive, broadband photodetectors, and image sensor

application. *Adv. Sci.* **6**, 1901134 (2019).
38. Venuthurumilli PK, Ye PD, Xu X. Plasmonic resonance enhanced polarization-sensitive photodetection by black phosphorus in near infrared. *ACS Nano* **12**, 4861-4867 (2018).
39. Zhao S, et al. Highly polarized and fast photoresponse of black phosphorus-InSe vertical p-n heterojunctions. *Adv. Funct. Mater.* **28**, 1802011 (2018).
40. Wu D, et al. Mixed-dimensional $PdSe_2$/SiNWA heterostructure based photovoltaic detectors for self-driven, broadband photodetection, infrared imaging and humidity sensing. *J. Mater. Chem. A* **8**, 3632-3642 (2020).
41. Bullock J, et al. Polarization-resolved black phosphorus/molybdenum disulfide mid-wave infrared photodiodes with high detectivity at room temperature. *Nat. Photon.* **12**, 601-607 (2018).
42. Wu D, et al. Highly polarization-sensitive, broadband, self-powered photodetector based on graphene/$PdSe_2$/germanium heterojunction. *ACS Nano* **13**, 9907-9917 (2019).
43. Sen P, et al. Panchromatic all-polymer photodetector with tunable polarization sensitivity. *Adv. Opt. Mater.* **7**, 1801346 (2018).
44. Periyanagounder D, et al. Fast-response, highly air-stable, and water-resistant organic photodetectors based on a single-crystal Pt complex. *Adv. Mater.* **32**, 1904634 (2019).
45. Horváth G, Wehner R. Skylight polarization as perceived by desert ants and measured by video polarimetry. *J. Comp. Physiol. A* **184**, 1-7 (1999).
46. Pomozi In, Horváth Gb, Wehner Rd. How the clear-sky angle of polarization pattern continues underneath clouds: full-sky measurements and implications for animal orientation. *J. Exp. Biol.* **204**, 2933-2942 (2001).
47. Barta A, Horvath G. Why is it advantageous for animals to detect celestial polarization in the ultraviolet? Skylight polarization under clouds and canopies is strongest in the UV. *J. Theor. Biol.* **226**, 429-437 (2004).